IN-32
85247

JPL Publication 87-16

81P.

Millimeter-Wave Imaging Sensor Data Evaluation

William J. Wilson
Anthony C. Ibbott

(NASA-CR-181159) MILLIMETER-WAVE IMAGING N87-26264
SENSOR DATA EVALUATION (Jet Propulsion
Lab.) 81 p Avail: NTIS HC A05/MF A01
CSCL 17B Unclas
G3/32 0085247

May 1, 1987

Prepared for

U.S. Army
Harry Diamond Laboratory

Through an agreement with

National Aeronautics and Space Administration

by

Jet Propulsion Laboratory
California Institute of Technology
Pasadena, California

JPL Publication 87-16

Millimeter-Wave Imaging Sensor Data Evaluation

William J. Wilson
Anthony C. Ibbott

May 1, 1987

Prepared for

U.S. Army
Harry Diamond Laboratory

Through an agreement with

National Aeronautics and
Space Administration

by

Jet Propulsion Laboratory
California Institute of Technology
Pasadena, California

The research described in this publication was carried out by the Jet Propulsion Laboratory, California Institute of Technology, and was sponsored by the U. S. Army, Harry Diamond Laboratory through an agreement with the National Aeronautics and Space Administration. This work was done under JPL Task Order No. RE-182 and Amendment No. 474, Change 1. This was funded by MIPR No. R-86-111.

ABSTRACT

A passive 3-mm radiometer system, with a mechanically scanned antenna, has been built for use on a small aircraft or an Unmanned Aerial Vehicle (UAV) to produce near-real-time, moderate-resolution (0.5°) images of the ground. One of the main advantages of this passive imaging sensor is that it is able to provide surveillance information through dust, smoke, fog, and clouds when visual and IR systems are unusable. This mm-wave imaging sensor can also be used for a variety of remote-sensing applications, such as measurements of surface moisture, surface temperature, vegetation extent, and snow cover. It is also possible to detect reflective objects underneath vegetation cover. The fact that the passive mm-wave sensor observes a different physical phenomenon makes it a valuable addition to visual, IR, and radar imaging systems.

A crosstrack scanning antenna system was used to scan a lightweight flat reflector ±20 degrees at a 4-Hz rate. A two-axis scanner, with gyro stabilization, was used to correct for aircraft motions due to turbulence and produced a raster scan pattern on the ground, which is well-suited for the real-time data display. At an altitude of 750 m (2,500 ft) with a forward velocity of 41 m/s (80 kts), a 0.5 x 1.3 km area is scanned in 32 seconds with a spatial resolution of 7 m.

Test flights were made in September 1985 and February 1986 with the sensor mounted on a commercial helicopter. The objectives of these test flights were to verify the capabilities of this sensor with respect to signal-to-noise ratio in operation with fog and clouds, and to get mm-wave imaging data on a variety of scenes and objects. These tests were very successful and examples of the imaging data are presented and described in this report. A number of image processing techniques have been used to bring out additional information in the images. An analysis of the sensor performance for detecting reflective objects in a variety of weather conditions is also presented. This analysis shows that the useful range of the sensor is greater than 750 m even through thick fog or clouds. A preliminary design for a UAV mm-wave sensor is also presented.

CONTENTS

CHAPTERS

Figures

Tables

CHAPTER 1. INTRODUCTION

A passive 3-mm radiometer system, with a mechanically scanned antenna, has been built for use on a small aircraft or helicopter to produce near-real-time, moderate-resolution images of the ground for Army surveillance applications. One of the main advantages of this passive imaging sensor is that it is able to provide valuable information through clouds, smoke, and dust when visual and IR systems are unusable. This sensor can also be used to detect metal objects under vegetation cover. This mm-wave imaging sensor is also useful for a variety of remote-sensing applications such as measurements of snow cover, surface moisture, vegetation extent, and surface temperature. Mapping fires and volcanic lava flows through obscuring clouds and smoke is also an application. The fact that the passive mm-wave sensor observes a different physical phenomenon, makes it a valuable addition to visual, IR and radar imaging systems.

When a mm-wave radiometer observes a ground scene from above, the received signal temperature is composed of emission from objects in the antenna beam, reflected sky emission, and atmospheric emission from the atmosphere below the radiometer. The received temperature from objects in the antenna beam is proportional to the product of its physical temperature and its surface emissivity. The surface emissivity is a function of the material and roughness, and ranges from near zero for reflectors, to near unity for absorbers. Thus, mm-wave scenes can show large contrasts with reflecting objects, such as metal vehicles, buildings or wet areas, appearing much colder than the surrounding rough background.

In the design of a mm-wave sensor for poor weather surveillance, the key factors are spatial resolution, low system noise, and low atmospheric emission and absorption. With the antenna size limited by aircraft constraints, the highest frequency will give the smallest spatial resolution. However, at higher frequencies, the poor weather atmospheric emission and absorption is larger and the receiver noise is higher. A trade-off study was done (see Chapter 5) and it was determined that for antenna diameters of 12-16 inches, the best system performance was in the atmospheric windows at 98 and 140 GHz. The 98-GHz frequency was chosen as the best system frequency, because more reliable and lower cost components are available. A description of the system is given in Chapter 2.

Test flights of the mm-wave imaging sensor were made in September 1985 and February 1986 with the sensor mounted on a commercial helicopter as shown in Fig. 1-1. Most of the flights were near an altitude of 750 m (2,500 ft)

Figure 1-1. Millimeter-wave imager shown mounted on the winglet of a Bell Jet Ranger helicopter. On the opposite winglet the 35-mm camera is mounted, and the video camera is mounted in front.

above ground level, and an air speed of ≈90 km/hr. The objectives of these test flights were to verify the capabilities of this sensor with respect to signal-to-noise ratio (SNR), operation with clouds, and to get mm-wave imaging data on a variety of areas and objects. These tests were very successful and examples of the data are shown in Chapter 3.

The mm-wave images have coarse spatial resolution when compared to optical or infrared images; however, there is a large amount of information which will be useful for surveillance applications during cloudy and foggy weather or through vegetation when the visual and IR images would be blank. A number of techniques can be used to extract additional information from the mm-wave images and examples are shown and discussed in Chapter 4.

An analysis of the performance of the sensor, based on the measured data, is given in Chapter 5. Curves of the expected SNR for tank detection for various weather conditions and antenna sizes are plotted vs range. Also included are images with reduced SNR to show the limitations of target detection. A preliminary design of the sensor for installation in an Unmanned Aerial Vehicle (UAV) is presented in Chapter 6 along with estimates of power and weight. Also included in this chapter are simulations of images using the reduced-size UAV sensor.

A number of presentations and publications have been given to describe the mm-wave imaging sensor and the results, and these are listed in Appendix A. A discussion of the jamming considerations is given in Appendix B.

CHAPTER 2. SYSTEM DESCRIPTION

The system configuration is shown in Fig. 2-1 and the system block diagram is shown in Fig. 2-2. A complete technical system description has been published in Ref. (1). A lightweight flat reflector is mechanically scanned crosstrack ±20 degrees at a 4-Hz rate. A two-axis scanner, controlled by a microcomputer with inputs from both rate and angle gyros, is used to scan the reflector and to correct for aircraft movement due to turbulence. This provides line-of-sight stabilization without the use of a conventional stabilized platform. The two-axis scanner also uses a butterfly scanning pattern to compensate for the forward aircraft motion to produce a linear raster scan pattern on the ground. The signal from the ground is reflected from the flat scanning mirror onto a 16-inch offset parabolic antenna which

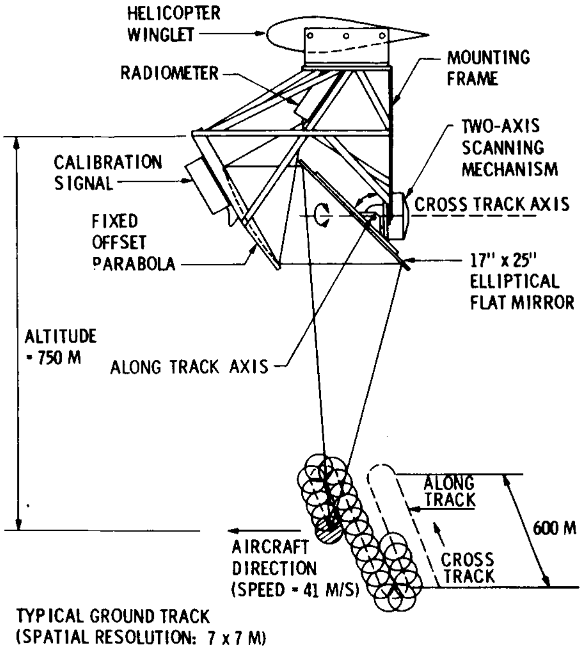

Figure 2-1. The system configuration of the mm-wave imaging sensor.

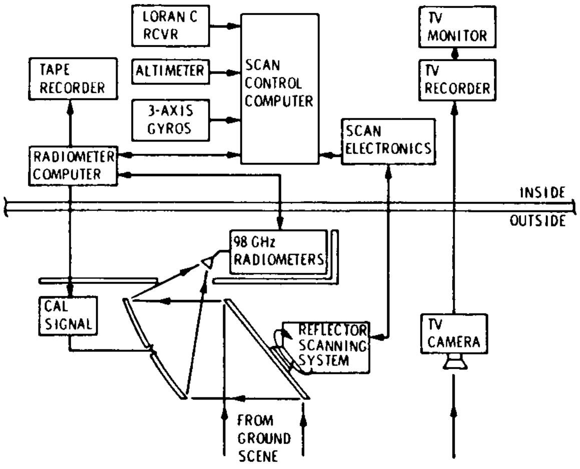

Figure 2-2. The block diagram of the mm-wave imaging sensor.

focuses the received signal on the radiometer's feed horn. An offset parabolic antenna was used for its high beam efficiency ($\eta > .9$) and low side lobes.

Two linearly polarized 98-GHz superheterodyne radiometers were used to provide polarization information and to improve the measurement sensitivity. A photograph of the radiometers is shown in Fig. 2-3 and a block diagram in Fig. 2-4. A broad-band orthomode junction splits the received signal into two orthogonal linearly polarized signals and the two radiometers use balanced mixers with beam-lead diodes. A Gunn diode oscillator, tuned to 98 GHz, is split with a hybrid tee and used to provide 2 mW of local oscillator power for each mixer. Each mixer is followed by a low-noise GaAs FET IF amplifier centered at 3 GHz. This mixer-preamp combination has an RF-to-IF gain of 34 dB and a double sideband (DSB) noise temperature of <750 K, measured at the mixer input. The measured DSB receiver temperatures, referenced to the feed horn, are 850 K and 1050 K for each receiver. The IF components following the mixer-preamp consist of another GaAs FET amplifier, a voltage-controlled pin diode attenuator, and a bandpass filter centered at 3 GHz with a 3-dB bandwidth of 2100 MHz. Following these components, a tunnel diode detector is used to convert the IF power to a low frequency signal. This output signal from each detector was amplified, integrated for ~0.5 ms, and then sampled with a sample-and-hold circuit. The signal was sampled at an interval corresponding to every one-half beamwidth on the ground. The sampled output signal was then sent to the radiometer computer, where it was digitized and converted to a brightness temperature. The rms noise per ground resolution element is <0.8 K when both radiometer channels are added. The radiometer box was temperature stabilized within ±2°C to reduce gain variations and to keep the receiver noise temperature constant.

ORIGINAL PAGE IS
OF POOR QUALITY

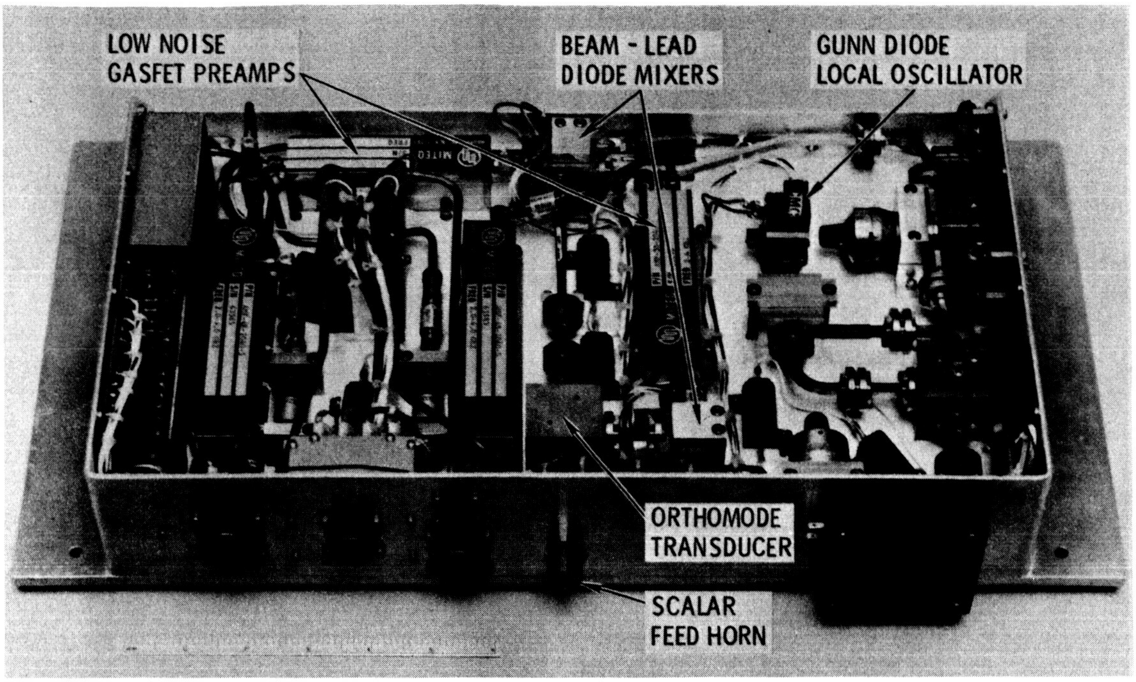

Figure 2-3. The 98-GHz dual polarized radiometers for the mm-wave imaging sensor. The chassis size is 14 x 9 x 3 inches.

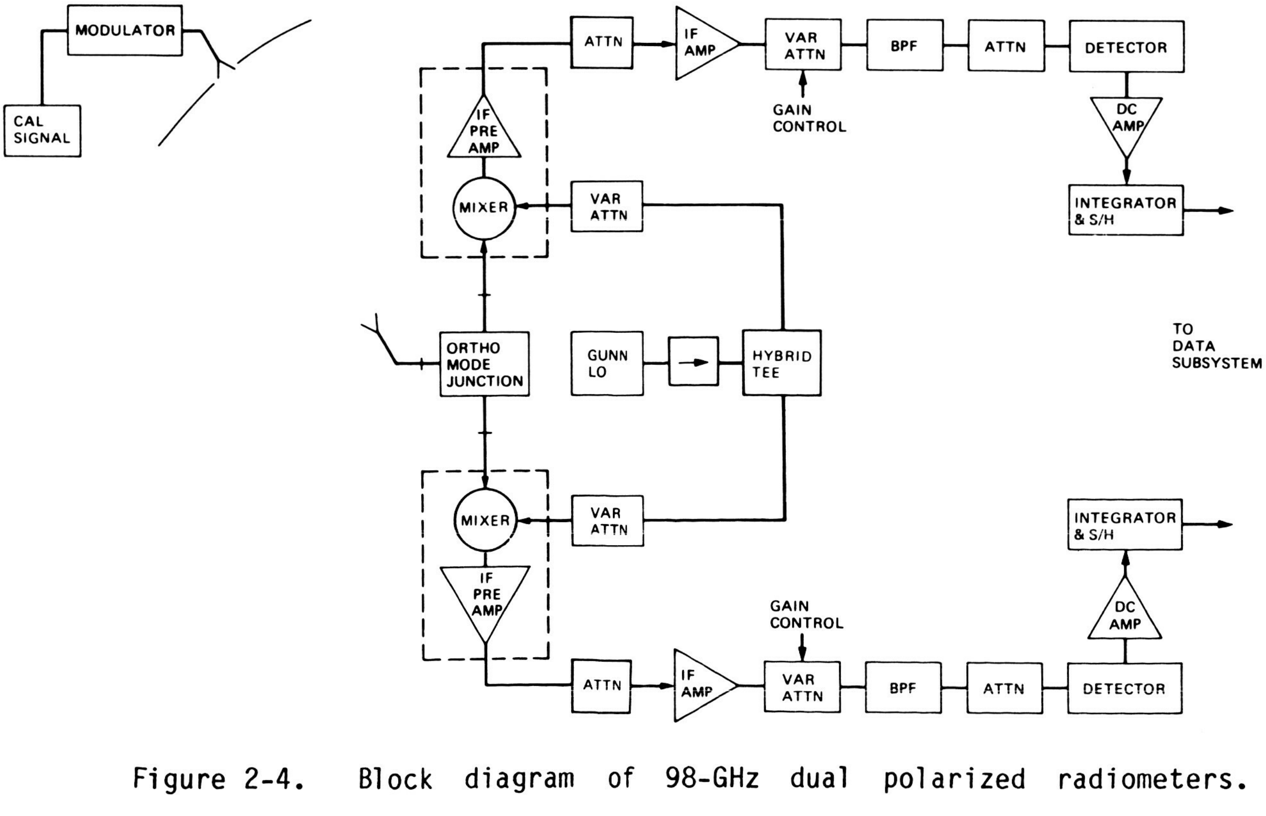

Figure 2-4. Block diagram of 98-GHz dual polarized radiometers.

Each radiometer is calibrated during the scanner's turnaround time at the end of each data line, which provides a calibration of the receiver gain every 125 ms. During the calibration period (~30 ms), the output of a 95-GHz Gunn diode calibration oscillator is modulated by the data system at ~1000 Hz and transmitted from the calibration box, through the central hole in the offset parabola, to the radiometer. This calibration signal is in the lower sideband of the radiometers; however, it was calibrated with thermal loads which have power in both sidebands. The calibration signal is polarized at a 45° angle to the radiometers' polarizations to provide nearly equal signals for each radiometer. The calibration box is temperature stabilized to within ±1°C to stabilize the calibration signal strength.

The output signals from the radiometer's microcomputer are recorded on a digital cartridge tape along with system status information. Ground truth data are given by a 35-mm camera (Nikon F with a 28-mm lens), a video camera (a miniature B & W Sony CCD (XC-38) with an 8.5-mm auto-iris lens) and in February 1985, an IR sensor (Inframetrics Model 102K). Because the data are taken with a stabilized raster pattern, the ground minicomputer system can immediately play back and display the data in false colors on a video monitor. The features that make this system unique from previous airborne mm-wave imaging sensors (Refs. 2-5), are its high resolution, small size, stabilization and computer processing to provide near-real-time calibrated images. Because of the stabilization and low data rate, this signal could be transmitted over a narrow-band channel (~50 kHz) for real-time display of the scene at a ground station.

The ground computer system for processing the data consists of a Hewlett-Packard A-700 minicomputer system and an RGB color monitor. The computer reads data from a source tape in the cartridge tape drive unit and displays the images on the color monitor. Numeric log information can be sent to the printer and a camera is used to make hard copies of the images.

The software processing functions are controlled by menus which allow selection of either radiometer channel, their sum or difference, and which specify offsets and scale factors. The displayed temperature range and the false color map can also be selected. There are two modes of image display: the first displays three columns consisting of approximately three minutes of data at a time, and the second displays enhanced images of 20 seconds of scene segments. In the enhanced mode, a scene is selected, and displayed in one screen quadrant along with a color histogram of the scene temperatures. The temperature range and colors can be adjusted and the scene redisplayed in an adjacent screen quadrant. The enhanced mode also allows for smoothing, edge enhancement and a zoom capability, and these techniques are discussed in Chapter 4.

REFERENCES

1. W. J. Wilson, R. J. Howard, A. C. Ibbott, G. S. Parks, and W. B. Ricketts, "Millimeter-wave Imaging Sensor," IEEE Trans. Microwave Theory Tech., Vol. MTT-34, p. 1026-1035, Oct. 1986.

2. J. P. Hollinger, J. E. Kenney, and B. E. Troy, Jr., "A Versatile Millimeter-wave Imaging System," IEEE Trans. Microwave Theory Tech., Vol. MTT-24, p. 786-793, Nov. 1976.

3. R. P. Moore, "Real-Time Microwave Radiometric Imager," Proc. of Society of Photo-Optical Instrumentation Engineers, Vol. 101, p. 6066, Apr. 1977.

4. B. Vowinkel, J. K. Peltonen, W. Reinert, K. Grüner and B. Aumiller, "Airborne Imaging System Using a Cryogenic 90 GHz Receiver," IEEE Trans. Microwave Theory Tech., Vol. MTT-29, p. 535-541, June 1981.

5. J. A. Gagliano and W. Gregorwich, "High-Altitude Atmospheric Measurements at 92/183 GHz Onboard the ER-2 Research Aircraft," in IEEE Proc. Eighth Int. Conf. on Infrared and Millimeter-waves, p. M6.8, Dec. 1983.

CHAPTER 3. SELECTED MILLIMETER-WAVE IMAGES

Over 20 hours of mm-wave imaging data were taken during the September 1985 and the February 1986 series of test flights. The objectives of these test flights were to verify the capabilities of this sensor with respect to SNR and operation with clouds, and to get mm-wave imaging data on a variety of scenes of cities, highways, farmland, water, and ships. These tests were very successful and 12 images have been selected, and are described in this chapter to illustrate the quality and variety of the mm-wave imaging data. The mm-wave images are displayed in false colors for easier interpretation. Beside each false color mm-wave image is a visual image - usually from the 35-mm camera, but sometimes from the TV camera. In Figures 3-10 and 3-11, the IR images are also included for comparison. All flights were near an altitude of 750 m (2,500 ft) above ground level, and an air speed of ~90 km/hr (~56 mph). A summary of the log data for these flights is given in Table 3-1. Some of the images shown in this chapter are used in later chapters to show other ways to display the data and to bring out additional information.

Figure 3-1 is an image of the 118 Freeway in Simi Valley, CA, just west of the Santa Susana Mountains. The helicopter was traveling west toward the Pacific Ocean. The coldest objects are the reflective metal objects which have a brightness temperature of ~80 K. The warmest objects are good absorbers at the ambient temperature of 300 K. This scene clearly shows the freeway, its intersections and the adjacent houses. Note that many of the vehicles on the roads in the visual image are shown in the mm-wave image. The differences are mainly due to the slightly different times of the video and mm-wave images. The speed of the helicopter was slightly faster than the traffic, thus vehicles moving in the same direction are stretched, and those moving in the opposite direction are shortened, or missed completely.

Table 3-1. Millimeter-Wave Image Data

Figure No.	Image	Date	Speed (mph)	Height Above Ground (feet)	Swath Width (feet)	Temperature Range (K) Lower	Temperature Range (K) Upper
3-1	Simi Valley Freeway	13-Sep-85	55	2400	1747	211	300
3-2(a,b)	Camp Pendleton buildings/hills	24-Sep-85	50	2800	2038	205	300
3-3	Fillmore citrus groves	19-Sep-85	55	2900	2111	228	300
3-4	Newport Bay	23-Sep-85	50	3300	2402	188	284
3-5	Ships in Long Beach Harbor	23-Sep-85	60	2500	1820	159	202
3-6	Tanks near Pulgas Lake	24-Sep-85	50	2619	1906	202	300
3-7	Camp Pendleton Field with tanks and landing pad	25-Sep-85	45	2500	1820	115	300
3-8	Brush fire at Camp Pendleton	25-Sep-85	60	2900	2111	260	460
3-9	Freeway with clouds	26-Sep-85	60	1800	1310	199	300
3-10	Airplanes at Mojave Airport	5-Feb-86	90	2641	1922	120	300
3-11	Agua Dulce Airport	5-Feb-86	55	2559	1862	234	300
3-12	Owens Valley Radio Observatory	5-Feb-86	50	2500	1820	80	289

Objects that can be seen in the mm-wave image but which are difficult to see in the visual image include:

- numerous swimming pools and spas in the backyards of houses on the left side of the freeway
- concrete slabs of new houses and tennis courts
- vehicles on the roads

Enough of the mm-wave features are recognizable, so that it is very easy to correlate it with the visual data.

Figures 3-2a and b are visual and mm-wave images of a coastal area in Camp Pendleton, CA. The buildings, parking lots and cars in the lower portion of Figure 3-2a appear much colder due to their higher reflectivity. Many dirt roads are also seen due to emissivity differences between them and the rougher land. If a lower range of temperatures is displayed, the rows of vehicles in the parking lots are easily seen, and there is much more detail shown in this complex of buildings (see Chapter 4). In the top part of the visual photograph in Fig. 3-2b are shown hills with shadows. These data were taken at 0823 hrs, and the mm-wave image clearly shows the cooler temperatures in the shadows. The asphalt road in the center of the image is ~15 K cooler than the surrounding background and there are several vehicles detected on this road. The cold objects in the center of Fig. 3-2b are power line towers and there is even a detection of a power transmission line across the center of this image.

Figure 3-3 is an image of an agricultural area west of Fillmore, CA and north of Sespe, CA. Most of the trees in this area are citrus and there is a dry river bed near the middle of the image. All the fields are clearly outlined; the cold areas in the fields are standing water and wet soil from irrigation. In the false color images, where this water really stands out,

Figure 3-1. Visual and mm-wave images of the 118 Freeway in Simi Valley, CA.

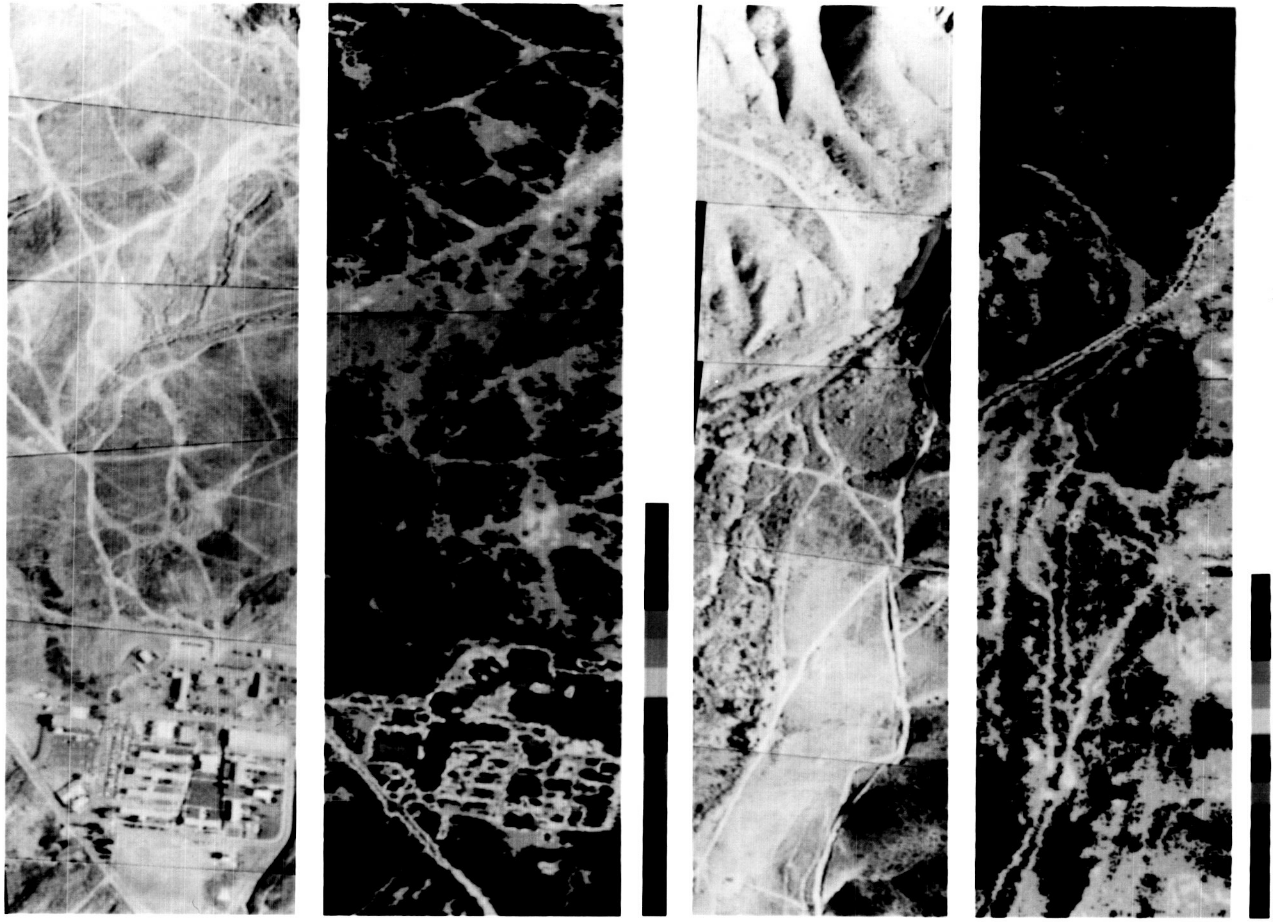

a

b

Figure 3-2. Visual and mm-wave images of a coastal area in Camp Pendleton, CA. (a) southern portion
(b) northern portion

it is very easy to see the wet soil, even through the vegetation. The small cold areas are storage tanks, vehicles and buildings. The warmest areas are ploughed fields and the dry river bed. Differences in the mm-wave image of fields are apparent even though the visual picture looks uniform. This is due to differences in the vegetation type and thickness, and soil moisture.

Figure 3-4 is an image of Newport Bay and its islands covered with houses. The aircraft was traveling southeast towards San Diego. A special distribution of colors was used to emphasize the small boats moored in the bay and the streets and houses on the islands. The boats are composed of wood and fiberglass and appear warmer than the reflective water.

Figure 3-5 is an image of larger ships (possibly oil tankers) in Long Beach outer harbor, just south of Terminal Island. Objects that can be seen in the mm-wave image but not in the visual image include hot spots toward the rear of the lower ship (possibly because of the engines), and cold spots elsewhere on the ship due to large metal surfaces. These surfaces are ~18 K cooler than the seawater, making the ships easy to detect against the sea surface which has very low clutter.

Figure 3-6 is an image of Army vehicles near Pulgas Lake, Camp Pendleton, CA. All the tanks and armored personnel carriers are detected in the mm-wave image. The SNRs were measured from these data and found to be ≈14 dB, which is in agreement with the calculations in Chapter 5. It should be noted that the brightness temperatures of the tanks were 260 ±10 K while the lake water was 202 ±2 K. Thus the tanks are easily distinguished from the lake and the 300 K background.

Figure 3-7 is an image of a field with many Army tanks and vehicles in Camp Pendleton. In the upper section of the image is the I-5 highway with

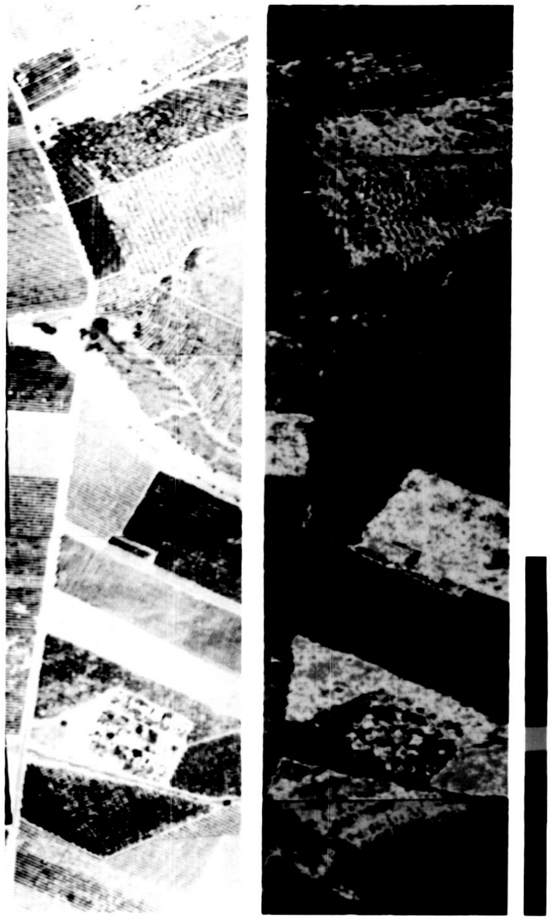

Figure 3-3. Visual and mm-wave images of an agricultural area west of Fillmore, CA and north of Sespe, CA.

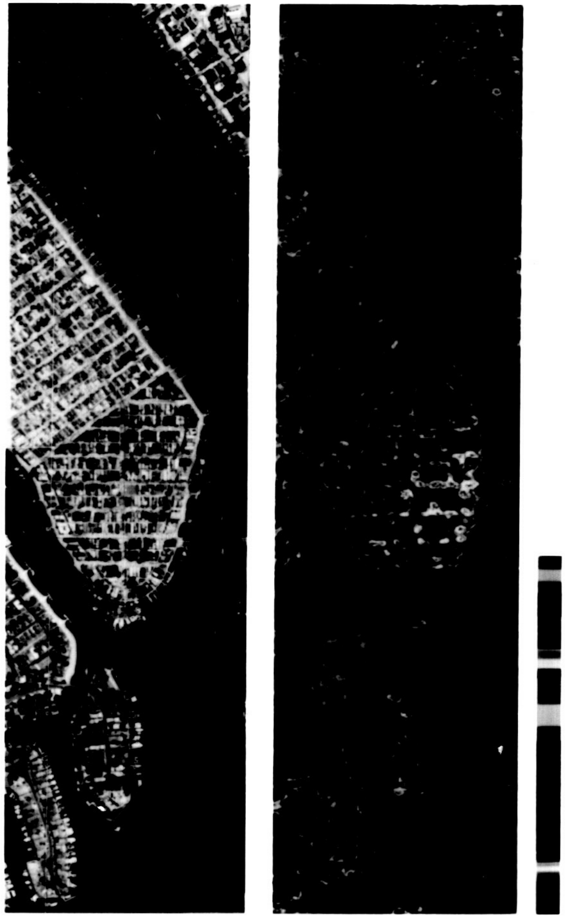

Figure 3-4. Visual and mm-wave images of Newport Bay and its islands covered with houses.

Figure 3-5. Visual and mm-wave images of large ships (possibly oil tankers) in Long Beach outer harbor, just south of Terminal Island.

vehicles and above this is a landing pad for aircraft. At the top of the picture is the ocean with waves that stand out due to their higher emissivity. Note that many of the land features (e.g., roads and hills) are seen in the mm-wave image making it easy to identify the scene. Also, the Army vehicles in the mm-wave image stand out while some of them are hard to see in the visual photograph.

Figure 3-8 is an image of a brush fire at Camp Pendleton. The fire appears to have burned an area between two dirt roads, and at the time the image was acquired, the fire area consisted of a great deal of ash and numerous hot spots. Several vehicles, both on and off the roads (presumably large fire trucks), are also detected.

Figure 3-9 is an image of the freeway south of Carlsbad, CA on September 26, 1985 during a cloudy, rainy day. During this day, the mm-wave sensor was flown at 1,800 ft above a layer of broken clouds which completely obscured the visual images over large areas. On the mm-wave image, the freeways, vehicles, parking lots, and buildings are clearly shown as colder targets, reflecting the cooler sky. As in Fig. 3-1, vehicles on the freeway, traveling in the same direction as the helicopter, have been stretched while those traveling in the opposite direction were compressed. This picture clearly shows the ability of the mm-wave imager to provide information on the ground scene when the scene is obscured by clouds.

Figure 3-10 is an image of the Mojave Airport. In this image, the helicopter was traveling northeast over a long line of large parked planes (Convair 990s). Due to strong winds, the aircraft was crabbing approximately 15 degrees to the left. In this figure, the left image is from the IR camera, next is a color 35-mm photograph, then the mm-wave image. In the IR image, the planes are shown cooler because it was a cool windy day. In the IR image,

ORIGINAL PAGE
COLOR PHOTOGRAPH

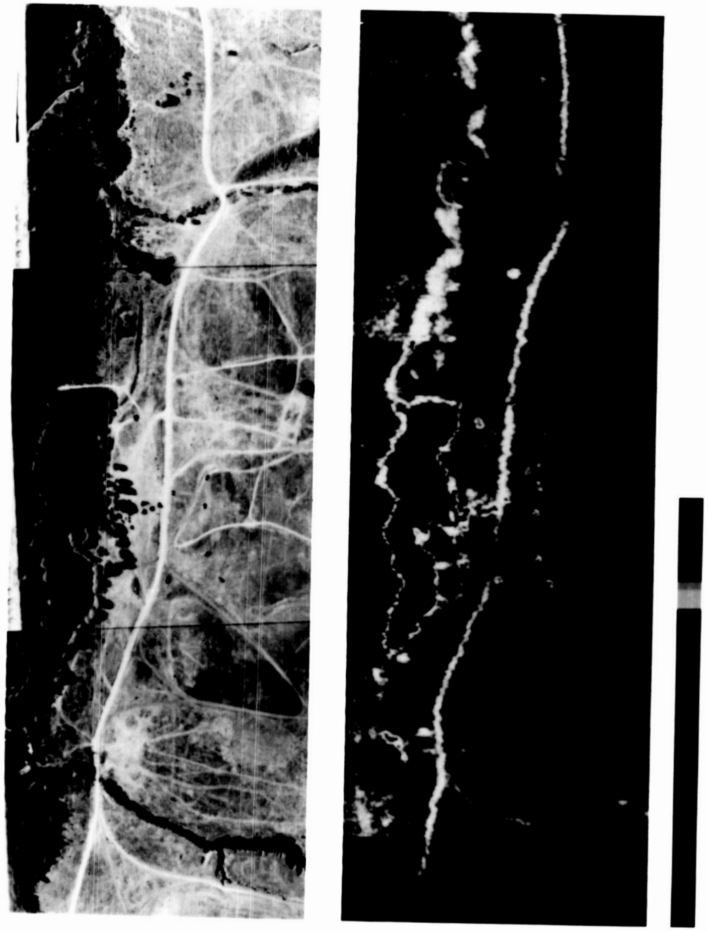

Figure 3-6. Visual and mm-wave images of Army vehicles near Pulgas Lake, Camp Pendleton, CA.

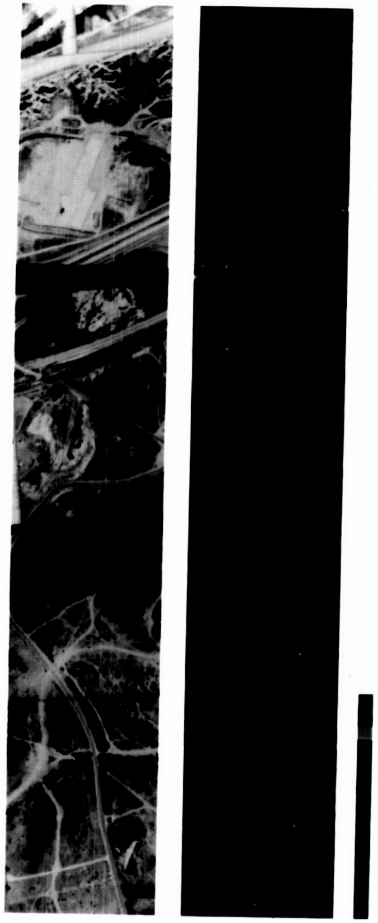

Figure 3-7. Visual and mm-wave images of a field with many Army tanks and vehicles in Camp Pendleton.

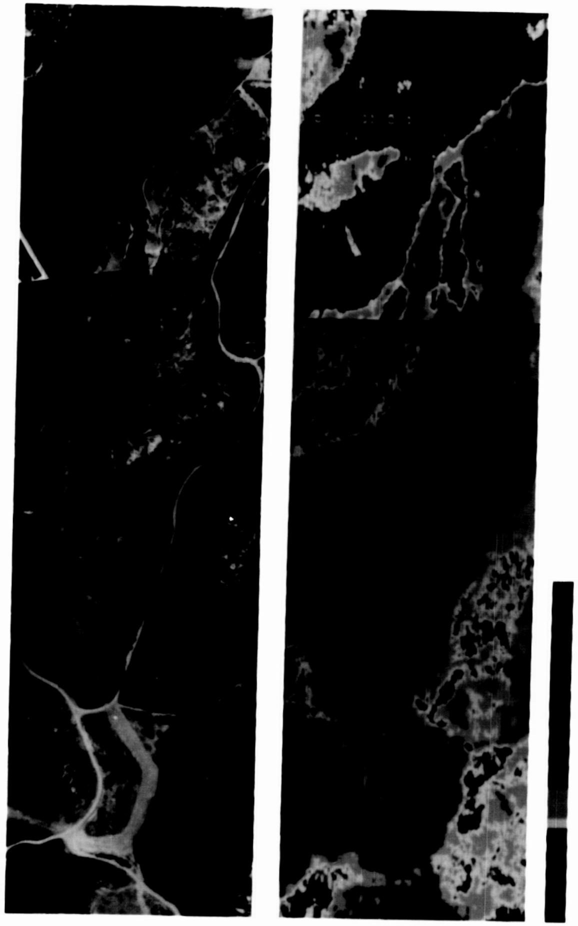

Figure 3-8. Visual and mm-wave images of a brush fire at Camp Pendleton.

ORIGINAL PAGE
COLOR PHOTOGRAPH

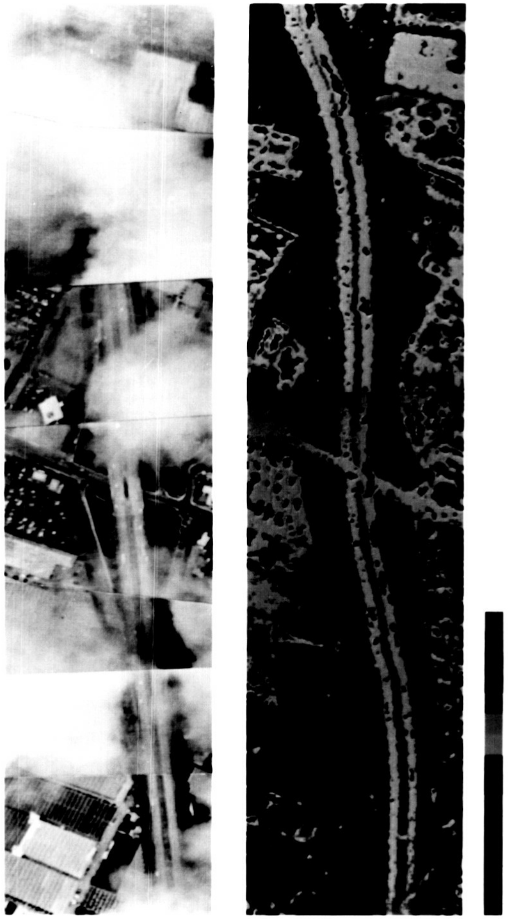

Figure 3-9. Visual and mm-wave images of the freeway south of Carlsbad, CA on a cloudy day.

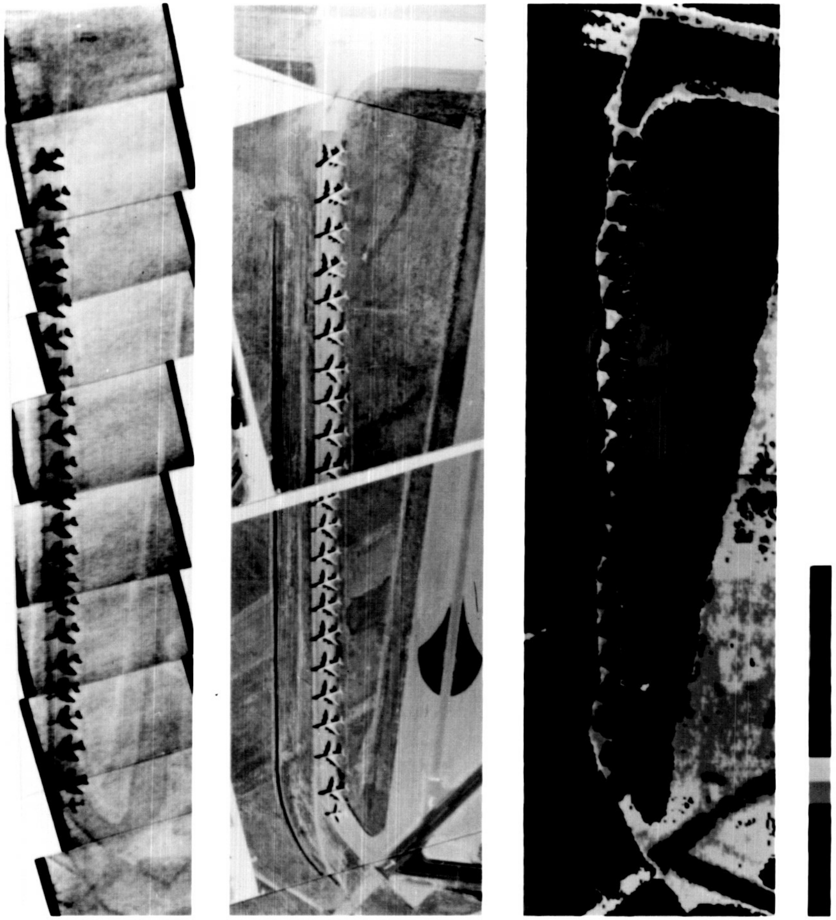

Figure 3-10. Infrared, visual and mm-wave images of the Mojave Airport.

it is difficult to see the runways because of the small temperature difference from the background. (Also note that the IR image has a narrower scan width than either the visual or the mm-wave images.) The mm-wave image clearly shows each aircraft with significant detail. The slight instability in the mm-wave image was due to the turbulence in the helicopter flight path. Note that the mm-wave image also shows significant detail in the ground around the aircraft due to grading or vegetation differences.

Figure 3-11 is an image of Agua Dulce Airport located in the Sierra Pelone Valley southwest of Palmdale, CA. As in Fig. 3-10, the left image is an IR picture and the second, a color 35-mm picture. Two mm-wave images are given with different color maps to emphasize different features. The reflective targets, buildings and airplanes are easily detected, along with the entire layout of the airport. The mm-image even detects the painted "22" on the runway. The small color shift in the middle of the picture is due to a radiometer gain change.

Figure 3-12 is an image of the Owens Valley Radio Observatory located between Big Pine and Bishop, CA. The Observatory has three large dish antennas spaced widely, and three small ones closer together easily seen in the mm-wave image, along with all the control buildings with metal roofs. Also note the sharp detail on the river.

**ORIGINAL PAGE
COLOR PHOTOGRAPH**

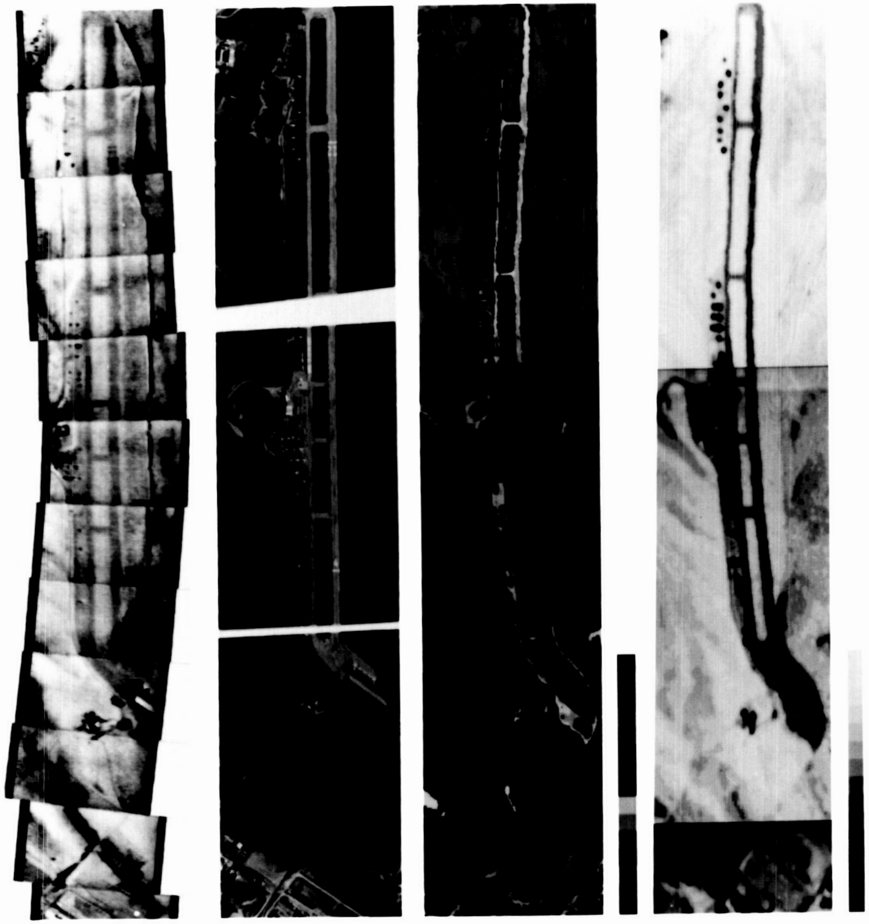

Figure 3-11. Infrared, visual and mm-wave images of Agua Dulce Airport located in the Sierra Pelone Valley southwest of Palmdale, CA.

Figure 3-12. Visual and mm-wave images of the Owens Valley Radio Observatory located between Big Pine and Bishop, CA.

CHAPTER 4. MILLIMETER-WAVE DATA ENHANCEMENT

INTRODUCTION

This chapter describes various image processing techniques which can be used on the mm-wave images to bring out additional details and information.

A. TEMPERATURE RANGE SELECTION

When displaying an image, the first choice is which range of temperatures to use. Because of the large contrasts in the mm-wave image, and the limited number of colors and color steps available, the range of temperatures must be chosen carefully to bring out different features. For example, choosing a low temperature range will bring out details in cooler reflective objects; whereas, choosing a high temperature range will bring out the details in the warmer background. Examples of how temperature range selection changes the image are shown in Figs. 4-1 through 4-4.

In the upper left (UL) image in each figure, the full expected range of brightness temperatures was used, 100-300 K. As can be seen in the histogram below the image, the majority of the pixels (picture elements) are between 250 and 300 K, which shows that only a few colors are used to display the image, and the others are unused. The only contrast that can be seen is where the temperatures cross the few color boundaries in use, consequently, much of the detail is lost. In the upper right (UR) image, the computer selected the temperature range based on displaying 95 percent of the data. This image is better but some details are lost in certain areas due to the large color steps. Pixels with temperatures outside the range are displayed by the end color. The lower left (LL) image has 2-K color steps in the low end of the temperature range showing the details in the cold targets, while the lower right (LR) image expands the upper end of the temperature range and provides details on the warmer objects.

ORIGINAL PAGE
COLOR PHOTOGRAPH

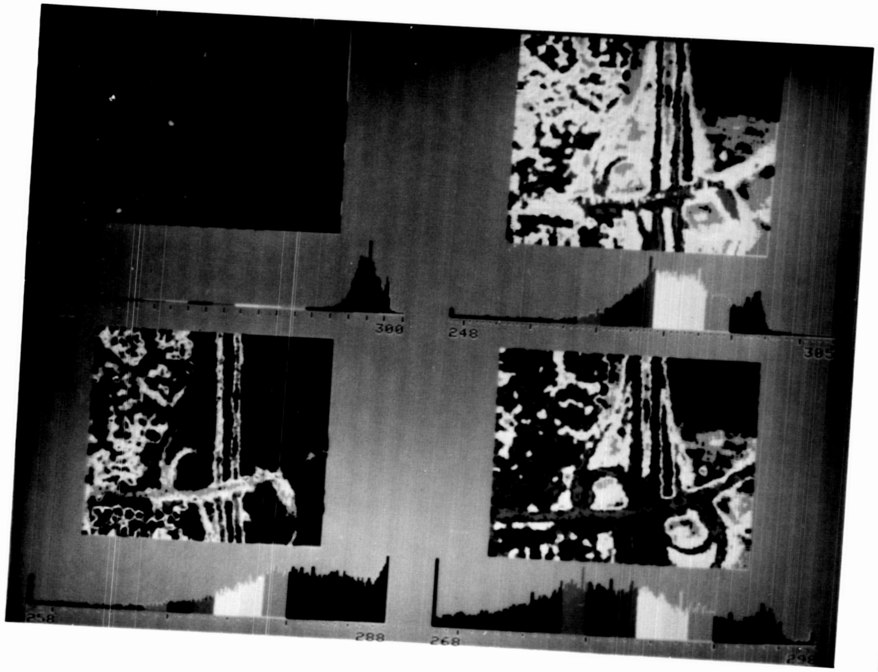

Figure 4-1. Example of how temperature range selection changes the appearance of an image of the 118 Freeway in Simi Valley, CA.

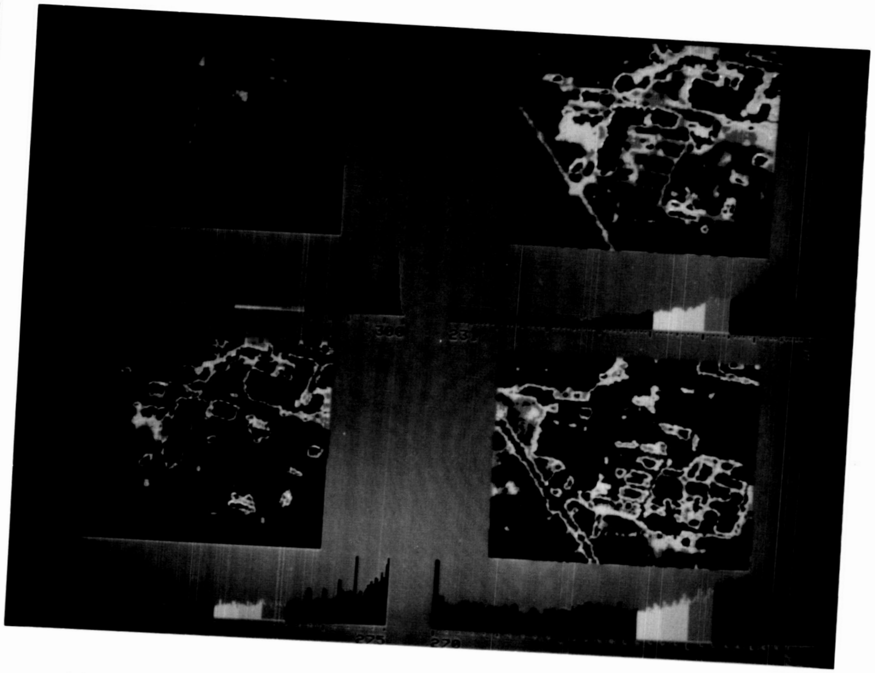

Figure 4-2. Example of how temperature range selection changes the appearance of an image of some buildings at Camp Pendleton, CA.

ORIGINAL PAGE
COLOR PHOTOGRAPH

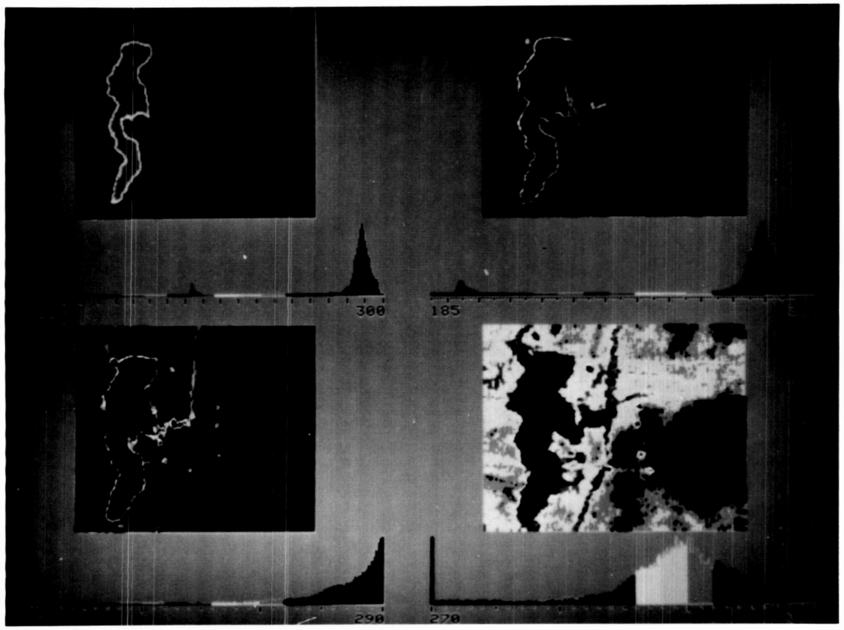

Figure 4-3. Example of how temperature range selection changes the appearance of an image of Pulgas Lake, Camp Pendleton, CA.

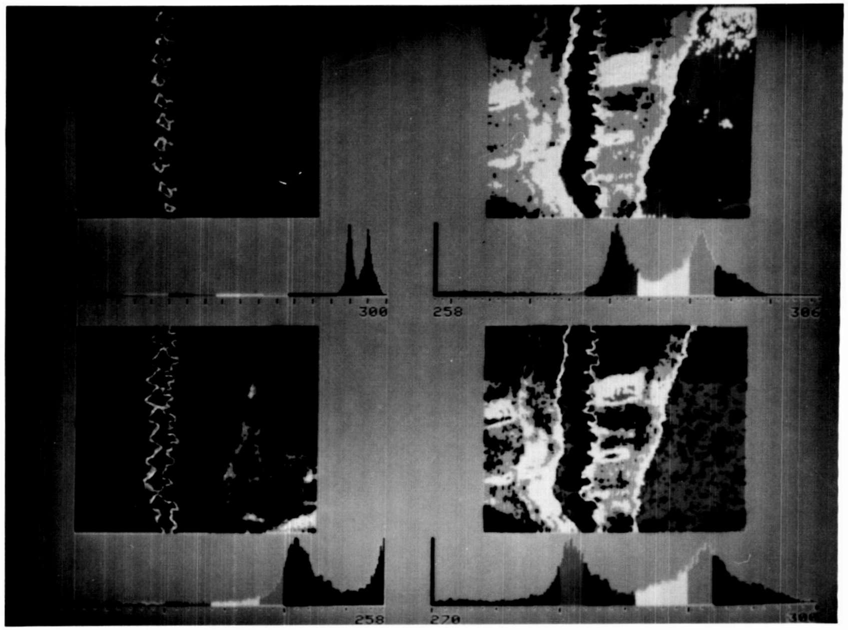

Figure 4-4. Example of how temperature range selection changes the appearance of an image of the Mojave Airport, CA.

In Figure 4-1, the Simi Valley Freeway scene (see Fig. 3-1), the best image for detection of vehicles is with the lower temperature range (LL), where the cold objects stand out against this background, although all three expanded range images show the vehicles. Additional cold objects that can be seen in the LL image include vehicles on the roads, concrete slabs of new houses, and swimming pools in the backyards of houses.

Figure 4-2 (see Fig. 3-2) shows the area of Camp Pendleton that includes a fire station and other buildings. However, the most prominent features are the rows of cars in the parking lots and the rows of tanks and other military vehicles near the top of the image. These can be most easily located in the LL and UR images as the dark blue areas.

Figure 4-3 shows the tanks near Pulgas Lake, Camp Pendleton (see Fig. 3-6). The numerous Army tanks and smaller vehicles are most visible in the LL image - the expansion of the colder range.

Figure 4-4 shows the Mojave Airport (see Fig. 3-10). Because the planes are very reflective, and parked on a warmer taxiway, they stand out nicely in all the images; however, the LR image gives the best details. As can be seen in Figures 4-1 to 4-4, it is helpful to display different temperature ranges to gain the most information from the image.

Based on a number of data flights, a study was made of the measured brightness temperatures for various types of objects in clear weather. A summary of this data is shown in Figure 4-5. In cases with reflective objects smaller than the antenna beam, the measured brightness temperatures will be higher, because the warmer background fills part of the beam. The coolest temperatures down to 80 K, are the large flat reflective objects such as water tanks, house trailers and large airplanes. In these cases the emission is mainly from the reflected sky. Objects with curved surfaces such as

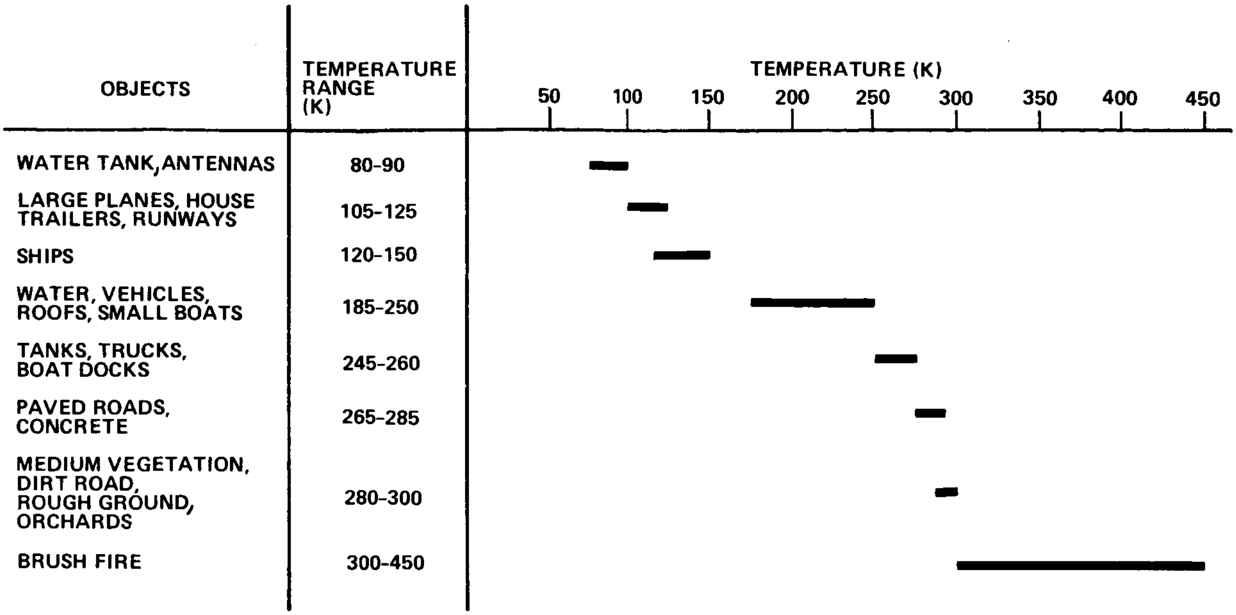

Figure 4-5. Measured brightness temperature at 98 GHz.

cars, trucks, boats and small planes are warmer -- in the range of 180-260 K. Water is in the range of 200-220 K; however, bodies of water can be distinguished because of their larger size. Military vehicles, such as tanks and trucks, are in the 250-265 K range -- much warmer than the water. Their warmer temperature is probably due to their curved surfaces reflecting the warmer background.

There is an overlap of the temperature ranges of various objects; however, from the temperature range, object locations and formations, it is possible to use this additional information to help determine the type of object. Having experience with this type of data will help in identifying various objects.

B. COLOR MAP SELECTION

After examining numerous mm-wave images, the following color map selection strategy has been found most useful. The first step is to display the image using a complete false color map from dark blue to bright red, with a contrasting dark color in the center of the color map -- see Figures 4-1 to 4-4. This provides an overview of the scene and allows identification of areas of most interest.

The next step is to display an image using only two colors; the lower half of the temperature range displayed with a light color and the upper half of the temperature range displayed with a dark color. By shifting the level between light and dark through the temperature range, the viewer can identify the major features of the image, as shown in Fig. 4-6.

Another technique is to display an image in all one color (such as white), and then change a small portion of the temperature range to a con-

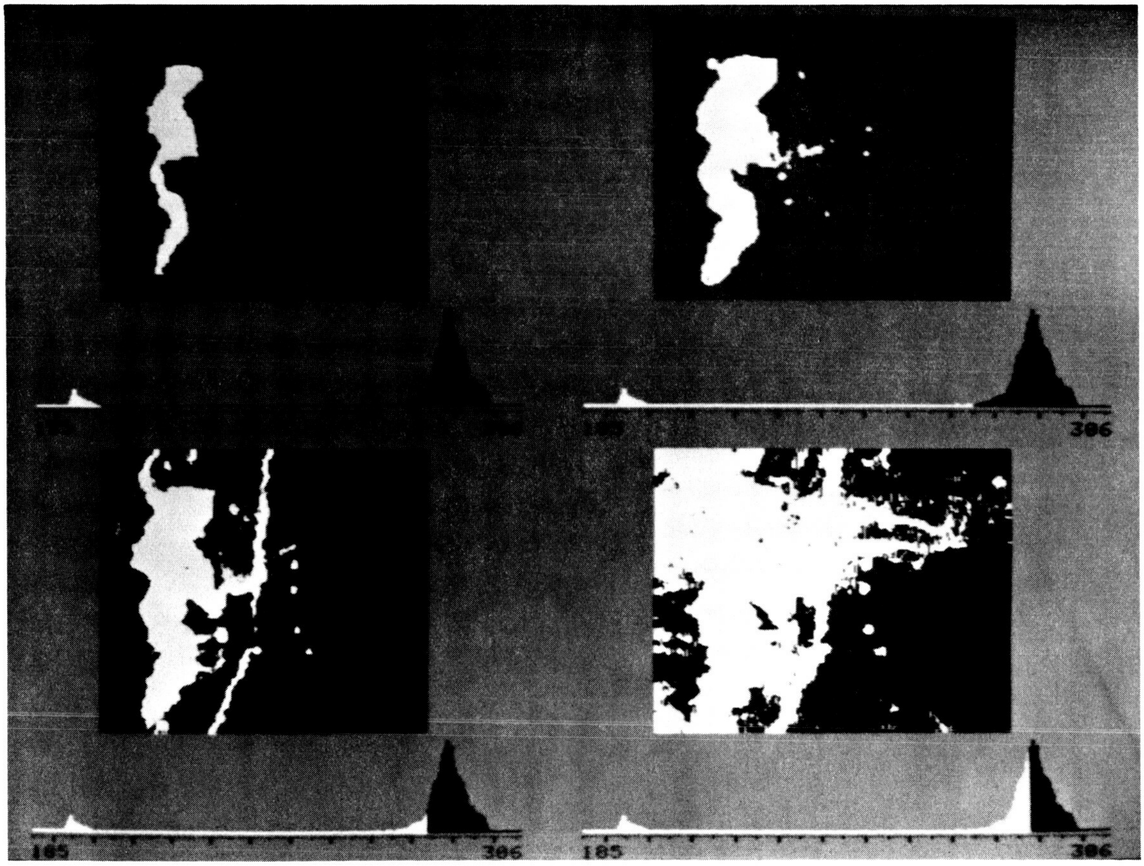

Figure 4-6. Four images of Pulgas Lake with various proportions of two colors. Note how the UR and LL images are most useful for detecting the outlines of prominent objects.

trasting color (such as pink). By shifting the contrasting color from one temperature step to another, specific features of the image become visible while all the rest are masked. This technique allows the viewer to locate areas of interest in silhouette and again not be distracted by excessive detail.

The fourth step is to use a gray scale ranging from black to white distributed across the temperature range. This allows the viewer to see all the features of the image at one time while still not being distracted by sharp color contrasts. This approach tends to make features blend in with each other and can even give the illusion of features similar to a black and white photograph. This is shown in Fig. 4-7 with the tanks at Pulgas Lake (see Fig. 3-7).

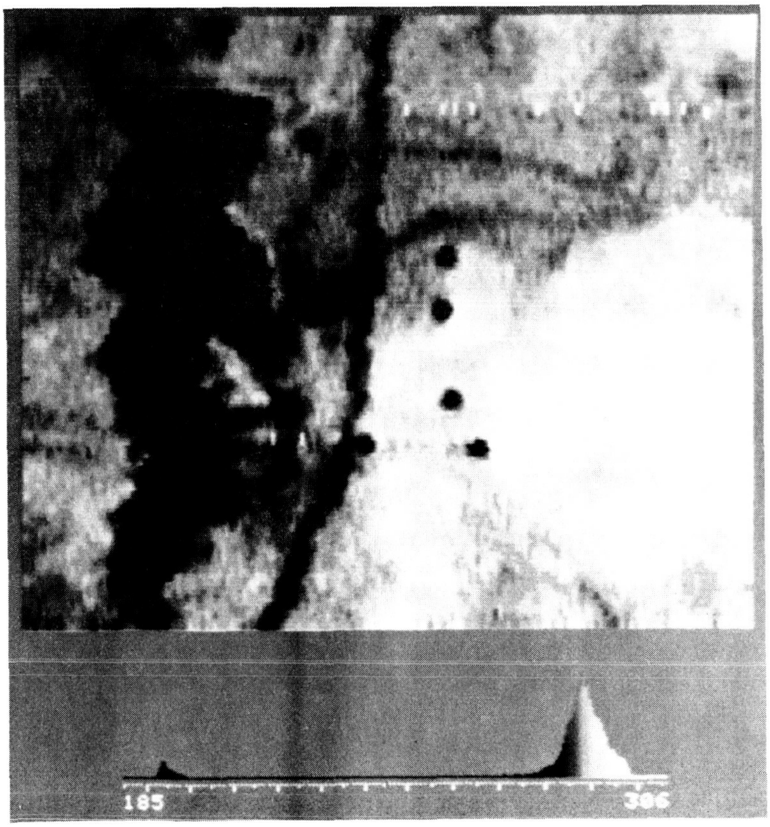

Figure 4-7. An image of Pulgas Lake using a gray scale. This appears similar to a black and white photograph.

An inverted gray scale provides another new perspective. This is similar to a black and white photographic negative where cold objects are displayed in white, and hot ones are displayed in black. By rapidly inverting the gray scale, the viewer can simulate a flickering black and white image and may discover that certain features catch his eye that had been previously overlooked (see Figure 4-8).

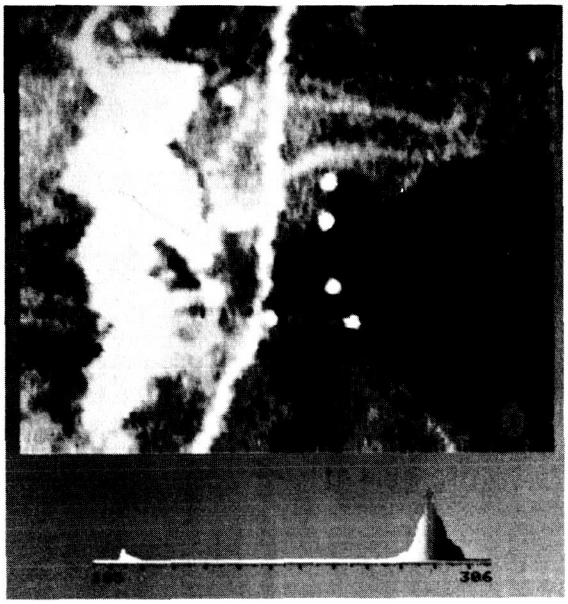

Figure 4-8. An image of Pulgas Lake using an inverted gray scale. Targets now stand out against the darker background.

To draw attention to specific details, the above techniques can be combined. This allows the viewer to see particular features that reside in the same portion of the temperature range (the contrasting color) while not losing reference points to the rest of the image (see Figure 4-9).

A rotating gray scale (whereby colors are rapidly shifted across the temperature range and wrap around to reappear on the other end) will provide the viewer with a sensation of movement. Hot and cold targets appear as either sources or drains of movement, depending on which way the color map is rotated (up or down the temperature range).

After viewing images this way, the viewer can also experiment with other mixtures of colors. Based on past experience a variety of color maps can be selected to bring out different details in the image. Images will still be recognizable when displayed by almost any combination of random colors. The fewer random colors there are (see Figure 3-5), the easier it is to recognize the image. The more random colors there are (up to 15 were tested), the more complex the image becomes.

An intelligent choice of colors is dependent upon what features the viewer wishes to make most prominent. For some images, a rainbow of colors will do the job. The most eye-appealing choice is to start with dark blue at the colder end of the temperature range, and progress up through several shades of blue, then into greens, browns, reds, and finally into orange, yellow, and white at the hottest end of the range. This has psychological appeal as most people subconsciously associate temperature and color in this manner. A dark contrasting color in the middle of the temperature range brings out details in the image.

For the most part, low temperature in the mm-wave image indicates a reflective or cold object (i.e., water). However, it is sometimes desirable to display such objects with a bright eye-catching color such as red or pink. For this reason, it was found that a frequently used color map was one composed of a short (10-color) gray scale covering the upper two-thirds of the temperature range, and shades of red, orange, and yellow covering the lower one-third of the range. In this way, the entire image is recognizable, and the cold reflective targets stand out. Likewise, hot targets can be made to stand out by using a gray scale for the lower two-thirds of the temperature range, and color shades covering the upper one-third of the range.

Now and then it is desirable to display an image with a special color map. An attempt can be made at pseudocoloring, i.e., blues for water, greens for vegetation, browns for bare Earth, and orange, yellow and white for concrete and other man-made objects. Unfortunately, this is usually not possible as the mm-wave brightness temperature of objects rarely conforms to such a coloring scheme. The best that can be hoped for is to develop a color map that will take into account the major features of the image without disguising too many of the minor ones. To this end, the most successful color maps are those which are a rainbow style but include a significant color contrast in the middle of the range such as a jump from light green to dark brown. This technique emphasizes one particular temperature boundary such as the difference between vegetation and a dirt road.

Another variable the viewer needs control over is the placement of the color boundaries. It turns out that the greater the number of colors used, the less difference it makes to shift the color boundaries. Conversely, the fewer colors used, the more necessary it is to be able to shift the boundaries of those colors to bring out details. For example, our image processing hardware uses 15 colors, and shifting the color temperature boundaries can usually improve images.

Several techniques exist for distributing colors across a temperature range. The first is that which has been assumed throughout this discussion, i.e., the 15 possible colors are spread evenly across the range. Another technique is to bunch some of them up at one end of the range thus increasing the definition of either the cold, or the hot targets (Figure 4-10). Additional techniques involve a histogram (a bar chart showing the quantity of pixels used to display each temperature segment of the image). The colors may be distributed in such a way that the same amount of each color is used

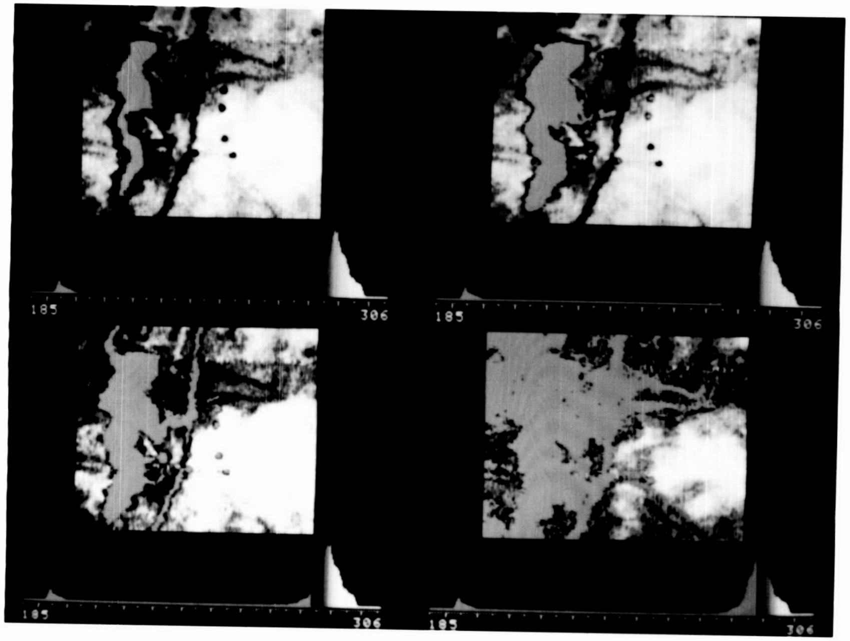

Figure 4-9. Four images of Pulgas Lake with a gray scale and various darker shades of gray changed to bright pink. This draws attention to the cold targets while not disturbing the rest of the image.

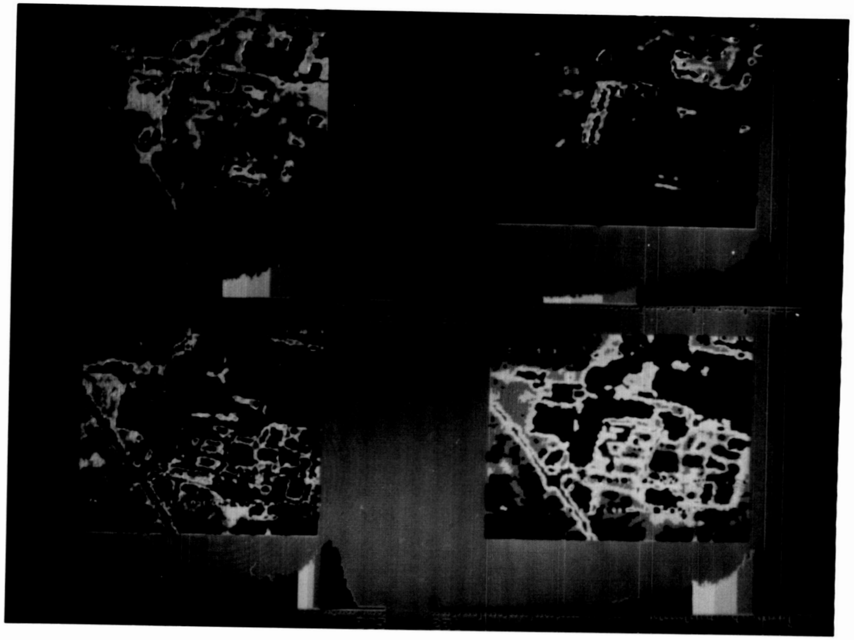

Figure 4-10. Four images of the buildings at Camp Pendleton, CA, using the same temperature selection, the same 15 colors, but with various distributions. Note how the image can be changed significantly.

in the image (i.e., the number of pixels of each color is equal). This has the effect of balancing the image somewhat. Another technique is to place more of the divisions on the peaks of the histogram, and fewer on the troughs. This has the effect of increasing the definition of the central temperatures of the image.

C. IMAGE FILTERS

Filtering an image can be useful to enhance a particular feature, or to suppress distracting features. The most useful filters for mm-wave images are those for smoothing, and for sharpening the edges of objects in an image.

Filters were applied to images by multiplying a three-pixel by three-pixel rectangle in the image with a corresponding three-pixel by three-pixel filter. The resulting nine values were added and the center pixel of the rectangle in the image was replaced by this sum. The process was repeated for each possible three by three rectangle.

Figure 4-11 shows an unfiltered image of Pulgas Lake. Images occasionally contained noise introduced by the imaging radiometer, or from the data acquisition computer. Some noise in an image can be reduced by a special filtering process. A pixel can be identified as noise if it is more than a predetermined temperature above or below the immediately surrounding pixels. If a pixel is identified as noise, it can be replaced by the average of the eight surrounding pixels. Noise that is not removed can cause problems because other filters tend to make the noise larger.

The mm-wave sensor has an oscillating mirror whereby rows of data pixels are acquired alternately from left to right, and from right to left. Under ideal conditions, the vertical alignment of pixels is correct. However,

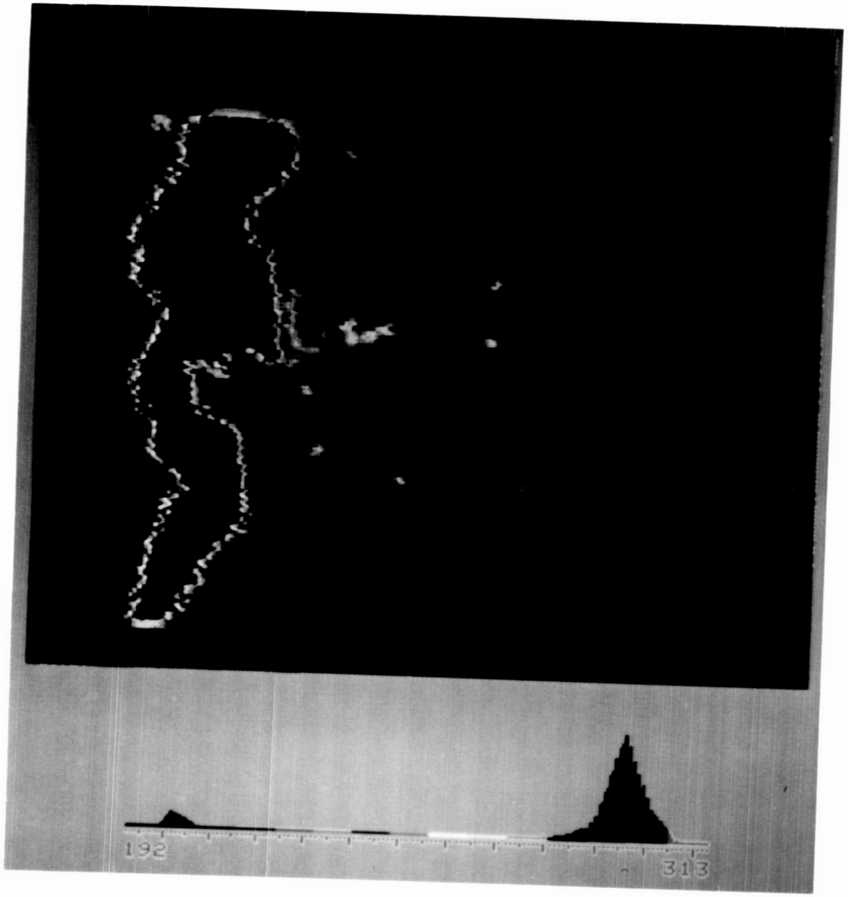

Figure 4-11. An image of Pulgas Lake with no filtering performed.

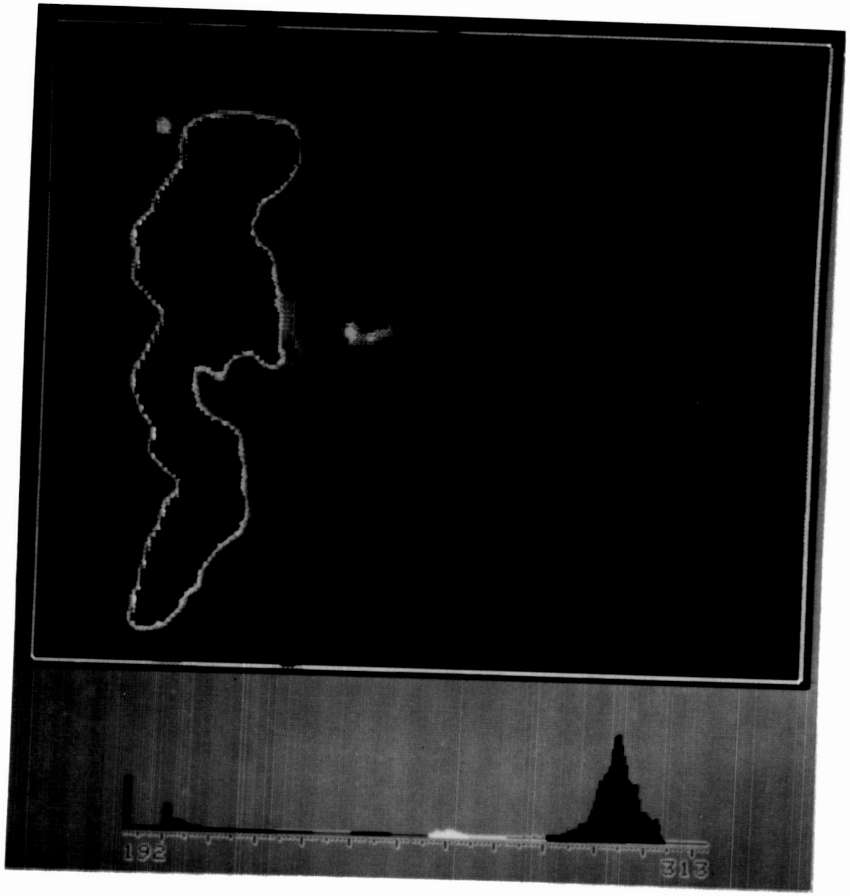

Figure 4-12. An image of Pulgas Lake after the noise removal, scan line removal, and smoothing filters have been applied.

sometimes aircraft motion and turbulence affect the mirror motion and a nonlinearity is introduced resulting in a one-half pixel zig-zag in the image. This jog from one row to the next in the image can be reduced by this filter:

$$\begin{matrix} 0 & .33 & 0 \\ 0 & .33 & 0 \\ 0 & .33 & 0 \end{matrix}$$

Effectively, each pixel is averaged with the one immediately above, and the one immediately below.

Images can be made to appear less noisy by smoothing them. One method to accomplish this is to apply the following averaging filter:

$$\begin{matrix} .111 & .111 & .111 \\ .111 & .111 & .111 \\ .111 & .111 & .111 \end{matrix}$$

This filter averages each pixel with its eight surrounding neighbors and results in a less 'choppy' image. Figure 4-12 shows an image after the above filters were applied. Note how this enhanced image makes it easier for the viewer to recognize terrain and identify targets.

Many of the images shown so far have used only 15 colors. This limitation is due to the hardware. When displaying an image in the smallest possible area on the screen, each pixel occupies only one spot on the screen, and thus can be only one of the 15 colors. By using four spots at a time for each data point, it is possible to display many more shades, e.g., combinations of the 15 colors. This technique is called dithering. The tradeoff is that the image occupies four times the space on the screen. Figures 4-11 and 4-12 are examples of dithering. The histogram is divided into blocks of the original 15 colors but each four-spot pixel in the image is one of 57 shades. For example, pixels in the center of the lake are 100% dark blue.

Toward the edge they are 75% dark blue/25% royal blue, followed by 50% dark/50% royal, then 25% dark/75% royal, and finally 100% royal blue. This technique is applied throughout the color map, resulting in a total of 57 combinations.

Figure 4-13 is the same image using only 15 colors. Note the lack of detail in the dirt roads around the lake.

The Sobel edge detection filter has been used successfully on several images (Figures 4-14 to 4-19), and works in the following manner:

$$\begin{array}{ccc} P1 & P2 & P3 \\ P4 & P5 & P6 \\ P7 & P8 & P9 \end{array}$$

$$X = (P3 + 2 \times P6 + P9) - (P1 + 2 \times P4 + P7)$$
$$Y = (P1 + 2 \times P2 + P3) - (P7 + 2 \times P8 + P9)$$

Then, the center pixel, P5 is replaced with the square root of X^2 plus Y^2. This has the effect of reducing the temperature of all the pixels, except those on the border of a temperature transition where the temperature is increased. The amount of the increase is proportional to the severity of the transition. Thus, cold spots turn into hot doughnuts and the colder the spot, the hotter the doughnut. Roads turn into two warm parallel lines. The main advantage of this filter is that it enhances small details that may not have been visible before, such as vehicles on flat ground.

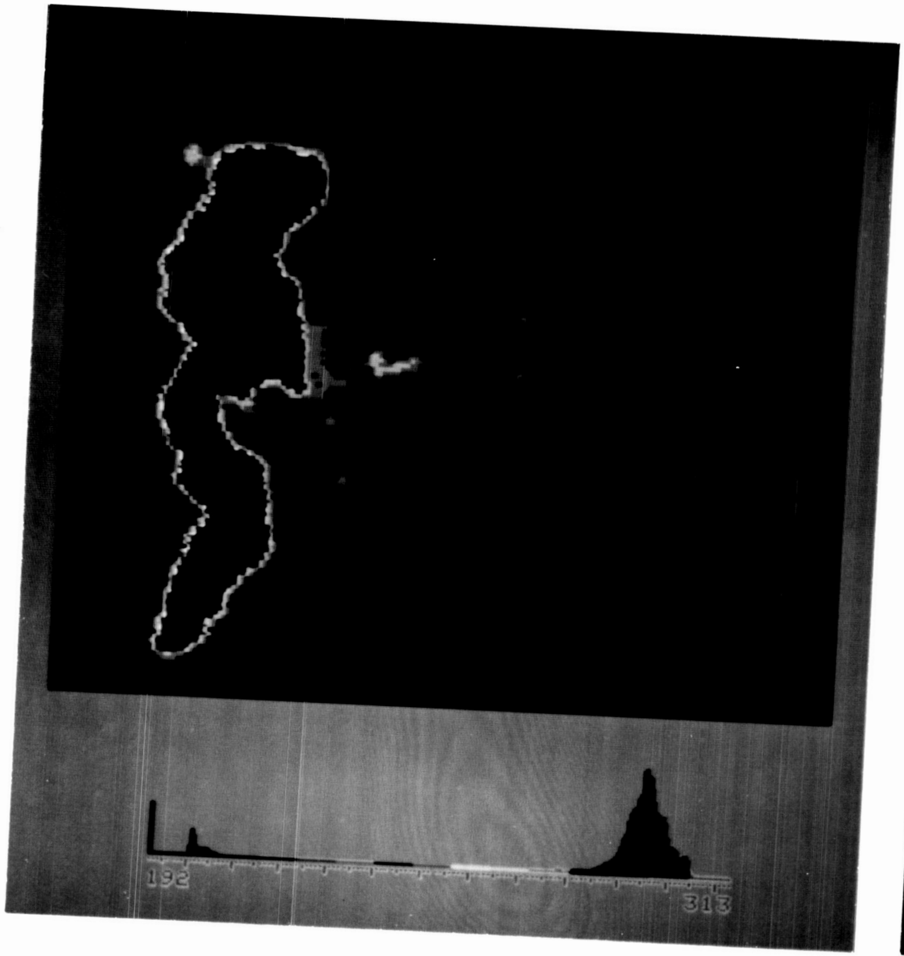

Figure 4-13. An image of Pulgas Lake using only 15 colors.

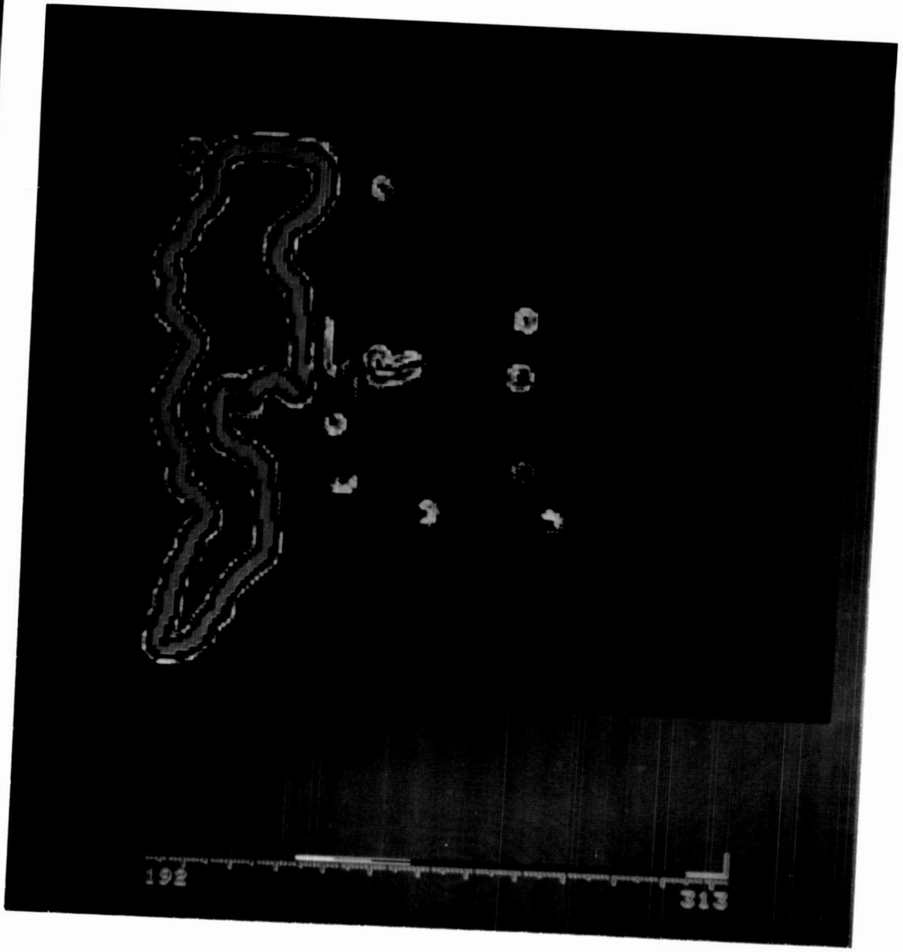

Figure 4-14. An image of Pulgas Lake after the Sobel edge detection filter has been applied.

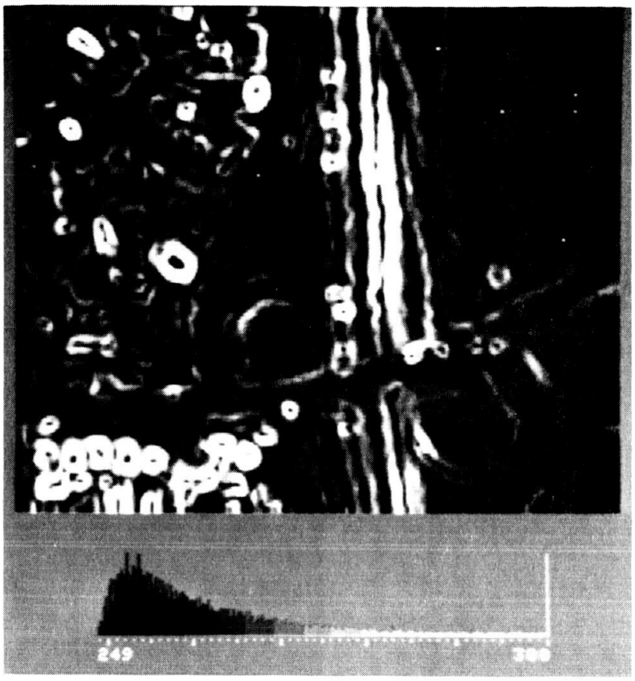

Figure 4-15. An image of the Simi Valley 118 Freeway after the Sobel edge detection filter has been applied.

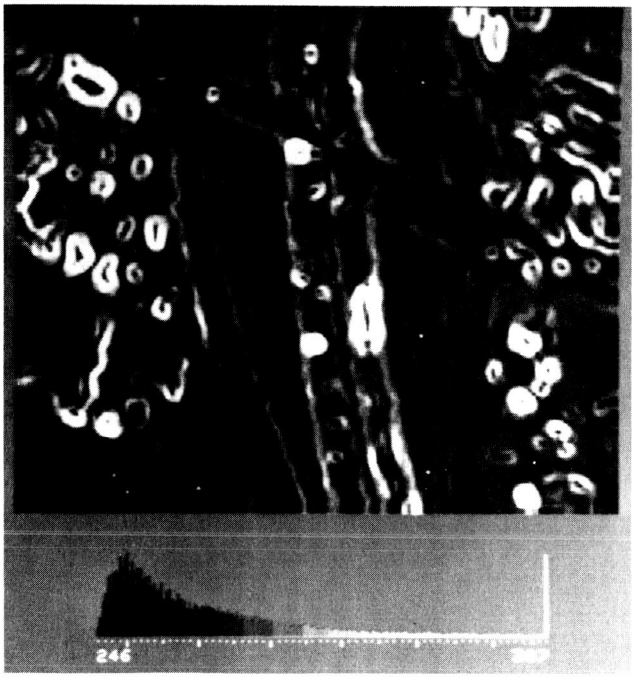

Figure 4-16. An image of the I-5 Freeway after the Sobel edge detection filter has been applied.

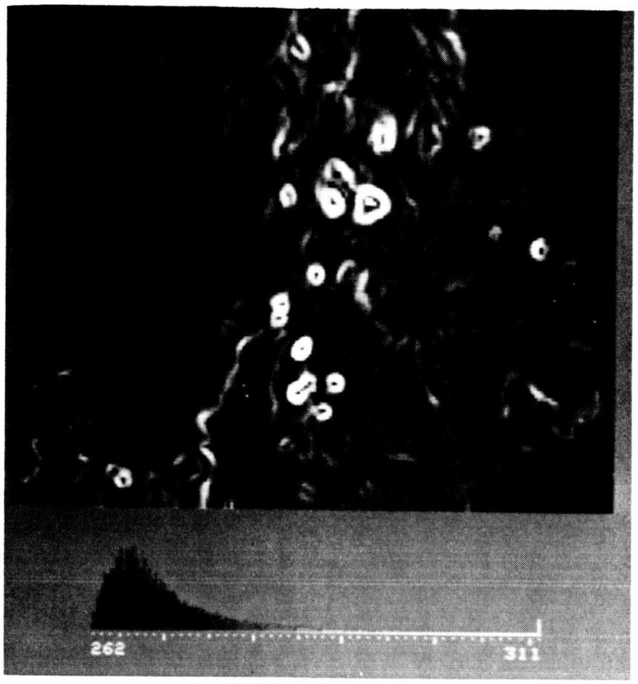

Figure 4-17. An image of the Camp Pendleton brush fire area after the Sobel edge detection filter has been applied.

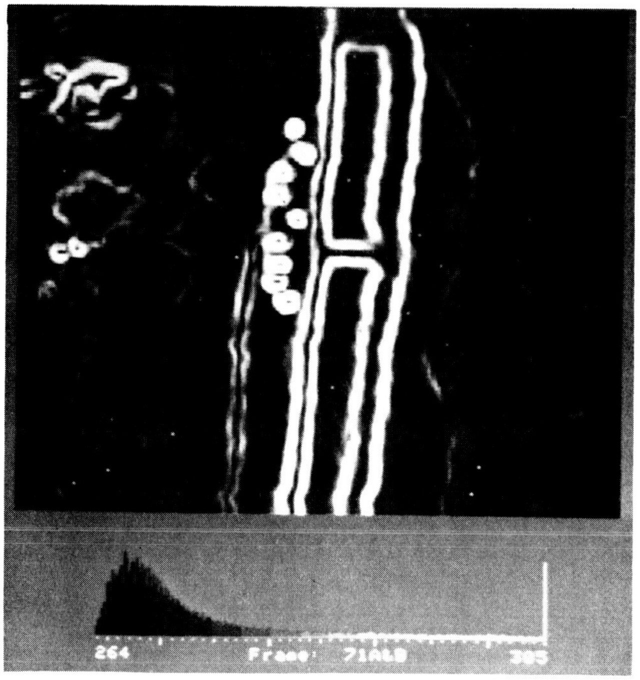

Figure 4-18. An image of the Agua Dulce Airport after the Sobel edge detection filter has been applied.

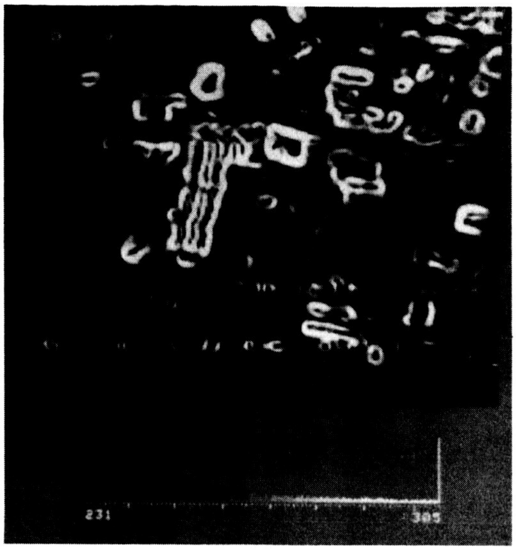

Figure 4-19. An image of the Camp Pendleton buildings after the Sobel edge detection filter has been applied.

D. OTHER SOPHISTICATED PROCESSING TECHNIQUES

Sophisticated image processing techniques that could be tried to further enhance the mm-wave data include using Fourier transforms for computing power spectra, Karhunen-Loeve transform, discrete cosine transform, and Walsh-Hadamard transform for feature classification, and the Kalman filter technique for feature extraction. Using these techniques, it is possible that the computer could be programmed to search for and recognize military targets. This could be done by searching for objects of certain temperatures, with certain sizes on certain terrains. The computer could even learn by searching for targets on its own, then signaling the operator when it found something that matched the broad pattern. If the operator verified that a target had been found, the target's characteristics could be added to the list of possible targets to look for in the future. The computer's broad pattern could be tailored by the learning process of being told what was, and what was not a valid target. Even multiple target formations could be recognized by the computer.

CHAPTER 5. ANALYSIS OF MILLIMETER-WAVE IMAGER PERFORMANCE IN DEGRADED WEATHER AND THROUGH VEGETATION

A. ANALYSIS IN DEGRADED WEATHER

When a mm-wave radiometer observes a ground scene from above, as shown in Fig. 5-1, the received signal temperature is composed of emission from objects and the background in the antenna beam, reflected sky emission from objects in the antenna beam, and atmospheric emission from the atmosphere below the radiometer:

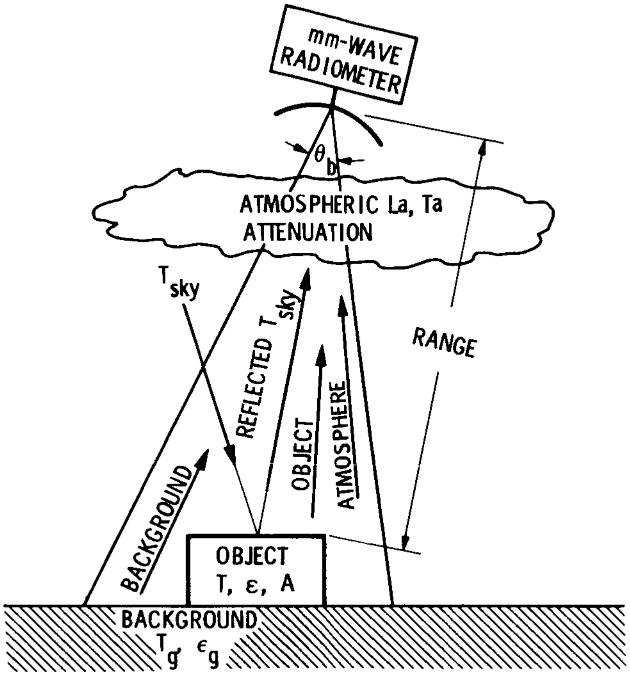

Figure 5-1. Millimeter-wave radiometer observing a ground scene from above.

$$T_{received} = T_{object} + T_{background} + T_{\substack{reflected\\sky}} + T_{atmos}\ (K) \qquad (1)$$

To simplify the equations, it has been assumed that all of the received power is within the main antenna beam, which is defined by the half-power beamwidth, Θ_b. (This is a good assumption for antennas with beam efficiencies of >90 percent used in imaging systems.)

The received temperature from an object in the antenna beam is equal to the product of the object's temperature and its emissivity, multiplied by the ratio of the object's area to the antenna's beam area and reduced by the atmospheric attenuation:

$$T_{object} = \frac{\varepsilon T \eta}{L_a} \quad (K) \qquad (2)$$

where:

ε = emissivity of the object ($0 < \varepsilon < 1$)

T = physical temperature of the object (K)

L_a = atmospheric absorption factor below the radiometer, i.e.,

$= 10^{(L_{atm} \cdot R/10^4)}$

L_{atm} = atmospheric attenuation (dB/km) below the radiometer

R = range to object (m)

η = ratio of objects area to main beam area ($0 < \eta < 1$)

$= \dfrac{A}{(\pi/4)\,(R \tan \Theta_b)^2}$

A = object's effective area (m^2)

Θ_b = antenna 3 dB beamwidth (deg)

The reflected sky emission temperature is equal to the product of the radiometric sky temperature and the quantity $(1 - \varepsilon)$ and is also multiplied by the ratio of the object's area to the antenna's beam area η, and reduced by the atmospheric absorption:

$$T_{\substack{reflected\\ sky}} = \frac{(1 - \varepsilon)\, T_{sky}\, \eta}{L_a} \quad (K) \qquad (3)$$

where:

T_{sky} = radiometric zenith sky temperature.

The received signal temperature from the background surrounding the object is given by:

$$T_{background} = \left(\frac{\varepsilon_g T_g + (1 - \varepsilon_g) T_{sky}}{L_a} \right) (1 - \eta) \qquad (4)$$

where

ε_g = emissivity of the background

T_g = physical temperature of the background

The atmospheric emission below the radiometer is:

$$T_{atmos} = T_a \left(1 - \frac{1}{L_a}\right) \qquad (5)$$

where T_a = physical temperature of the atmosphere below the radiometer.

Values of L_{atm} and T_{sky}, for a variety of weather conditions, are shown in Table 5-1 for three mm-wave atmospheric "window" frequencies, e.g., 98, 140 and 220 GHz. These data were summarized from a selection of propagation work (Refs. 1-6) and represent "best guess" averages for the specified weather

Table 5-1. Millimeter-Wave Atmospheric Parameters vs Weather

		98 GHz		140 GHz		220 GHz	
Case	Weather Conditions	Latm (dB/km)	Tsky (K)	Latm (dB/km)	Tsky (K)	Latm (dB/km)	Tsky (K)
1	Clear (7.5 g/m^3, 50% RH), Moderate Fog, Smoke, Dust	0.4	50	1.2	110	3.5	170
2	Clear (12 g/m^3, 100% RH), Thick Fog	0.8	80	1.5	120	4.0	190
3	Overcast, Cloud (.5 km thick), Dense Fog	1.2	150	2.0	180	5.0	200
4	Light Rain <4 mm/hr	1.6	200	2.4	220	5.5	230

conditions. These data are representative of the range of conditions under which the mm-wave sensor could be operated. In Case 4, light rain, it was estimated that the emissivity of the wet background would decrease from 0.95 to 0.5; however, further measurements will be required to verify this estimate.

Since the received temperature from the object in the antenna beam is proportional to the product of its physical temperature and its surface emissivity, as shown in Eq. (2), reflective objects (metal or water) will appear colder than the surrounding high-emissivity background (soil or vegetation). Thus, mm-wave images can show large contrasts, because the reflective objects will "stand out" from the background with a large temperature difference or SNR. Using the data in Table 5-1, and values of other parameters shown in Table 5-2, the expected signal and the SNR for a tank vs range were calculated and are shown in Table 5-3.

B. CALCULATED RESULTS

The expected signal is given by the expression:

$$T_{signal} = T_{received}\ (\text{with tank}) - T_{received}\ (\text{without tank}) \qquad (6)$$

and the SNR is:

$$SNR = 10 \log \left(\frac{T_{signal}}{T_{noise}} \right) \qquad (7)$$

The noise is made up of two independent components, radiometer noise and image clutter noise.

$$T_{noise} = (T_{rad}^2 + T_{clutter}^2)^{1/2} \ . \qquad (8)$$

For our dual channel, mm-wave total power radiometer with a noise temperature of ≈900 K (DSB), observing a 290 K background, with a bandwidth of 2 GHz and integration time per pixel of 0.5 msec, the radiometer noise

Table 5-2. Parameters Used in Calculation of T_{signal} and SNR

Target Area (A) = 10 m^2 (see text)
Target Emissivity (ε) = 0.3 (Case 4, $\varepsilon = 0.15$)
Target Temperature (T) = 305 K

Background Emissivity (ε_g) = 0.95 (case 4, $\varepsilon_g = 0.5$)
Background Temperature (T_g) = 295 K
Atmospheric Temperature (T_a) = 290 K

T_{rad} (98 GHz) = 0.8 K
T_{rad} (140 GHz) = 1.3 K
T_{rad} (220 GHz) = 1.9 K

Table 5-3. Millimeter-Wave SNR for Tank Detection

98 GHz 16-in. Antenna

	CASE 1		CASE 2		CASE 3		CASE 4	
RANGE	Tsig	SNR(dB)	Tsig	SNR(dB)	Tsig	SNR(dB)	Tsig	SNR(dB)
0.5	93	17.6	77	16.8	49	14.9	16	10.1
0.75	40	14.0	33	13.1	20	11.1	7	6.2
1.0	22	11.4	18	10.4	11	8.3	3	3.3
1.25	14	9.4	11	8.3	6	6.0	2	0.9
1.5	9	7.7	7	6.5	4	4.1	1	-1

140 GHz 16-in. Antenna

	CASE 1		CASE 2		CASE 3		CASE 4	
RANGE	Tsig	SNR(dB)	Tsig	SNR(dB)	Tsig	SNR(dB)	Tsig	SNR(dB)
0.5	102	17.3	93	16.9	57	14.7	19	9.9
0.75	54	14.5	48	14	29	11.7	9	6.8
1.0	28	11.7	25	11.1	14	8.8	5	3.7
1.25	17	9.4	15	8.8	8	6.3	3	1.2
1.5	11	7.6	9	6.9	5	4.2	2	-1

220 GHz 16-in. Antenna

	CASE 1		CASE 2		CASE 3		CASE 4	
RANGE	Tsig	SNR(dB)	Tsig	SNR(dB)	Tsig	SNR(dB)	Tsig	SNR(dB)
0.5	52	13.4	41	12.3	33	11.4	11	6.7
0.75	43	12.5	33	11.3	25	10.1	8	5.4
1.0	27	10.6	20	9.3	15	7.8	5	2.9
1.25	14	7.8	10	6.3	7	4.6	2	-0.4
1.5	8	5.3	6	3.8	4	1.8	1	-3.4

98 GHz 12-in. Antenna

	CASE 1		CASE 2		CASE 3		CASE 4	
RANGE	Tsig	SNR(dB)	Tsig	SNR(dB)	Tsig	SNR(dB)	Tsig	SNR(dB)
0.5	52	15.1	44	14.3	28	12.4	9	7.6
0.75	23	11.5	18	10.6	12	8.6	4	3.7
1.0	12	8.9	10	7.9	6	5.8	2	0.8
1.25	8	6.9	6	5.8	4	3.5	1	-1.6
1.5	5	5.2	4	4	2	1.7	1	-3.5

140 GHz 12-in. Antenna

	CASE 1		CASE 2		CASE 3		CASE 4	
RANGE	Tsig	SNR(dB)	Tsig	SNR(dB)	Tsig	SNR(dB)	Tsig	SNR(dB)
0.5	73	15.8	66	15.4	41	13.3	13	8.4
0.75	30	12.0	27	11.5	16	9.3	5	4.3
1.0	16	9.2	14	8.6	8	6.3	3	1.2
1.25	9	6.9	8	6.3	5	3.8	1	-1.3
1.5	6	5.1	5	4.4	3	1.7	1	-3.5

220 GHz 12-in. Antenna

	CASE 1		CASE 2		CASE 3		CASE 4	
RANGE	Tsig	SNR(dB)	Tsig	SNR(dB)	Tsig	SNR(dB)	Tsig	SNR(dB)
0.5	52	13.4	41	12.3	33	11.4	11	6.7
0.75	33	11.4	26	10.3	19	9.1	6	4.3
1.0	15	8.1	11	6.8	8	5.3	3	0.4
1.25	8	5.3	6	3.8	4	2.1	1	-2.9
1.5	5	2.8	3	1.3	2	-0.7	1	-5.9

per pixel is T_{rad} = 0.8 K. Based on our September data for open field areas, as shown in Section 5B, the rms clutter noise was ≈1.4 K. Thus the total noise is ≈1.6 K for the 98-GHz system. At the higher frequencies where receivers are worse, the radiometer noise would be larger and the values in Table 5-2 were used.

The signal values in Table 5-3 were calculated for both a 12- and 16-inch diameter antenna system. The curved and slanted surfaces on the tank do not reflect all the sky radiation to the radiometer, which effectively reduces its area. Thus the effective tank area, used in the calculations, was reduced to ≈40 percent of the physical area to obtain agreement with the measured September 1985 data. (A detailed study of radiometric imaging of tanks has been reported in Ref. 7.) The data in Table 5-3 has been plotted in Figures 5-2 to 5-4, and a line has been drawn at an SNR of 7 dB to show the region of >5 sigma detection.

These data show that the 98-GHz mm-wave sensor with a 16-inch antenna will detect objects, such as tanks, up to ranges of 1.5 km under conditions of light and moderate fog, dust or smoke. Under moderate overcast, thick fog and even thick clouds, targets can be detected up to ranges of 1.2 km. For the limiting conditions of light rain and L_{atm} = 1.6 dB/km, the effective range would be up to 700 m. The results are similar using 140 GHz; however, at 220 GHz the SNRs are ≈2 dB lower, making this frequency undesirable. With a 12-inch-diameter antenna, tanks can be detected up to ranges of 1 km in all the weather conditions without rain at both 98 and 140 GHz. Again the 220-GHz results are ~2 dB worse.

Even though the 140-GHz SNR results are slightly better than the 98-GHz results, it is recommended that mm-wave imaging sensors be built using 98 GHz since more reliable and lower cost components are available at 98 GHz. Using image processing methods as discussed in previous chapters,

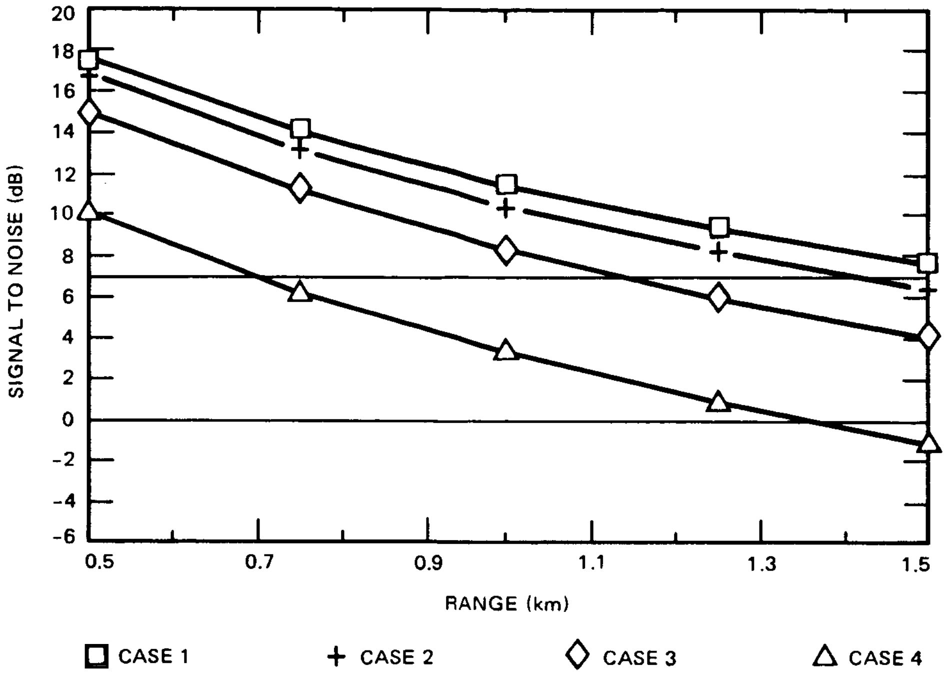

Figure 5-2(a). Millimeter-wave imaging sensor - calculated performance for 98 GHz with a 16-inch-diameter antenna.

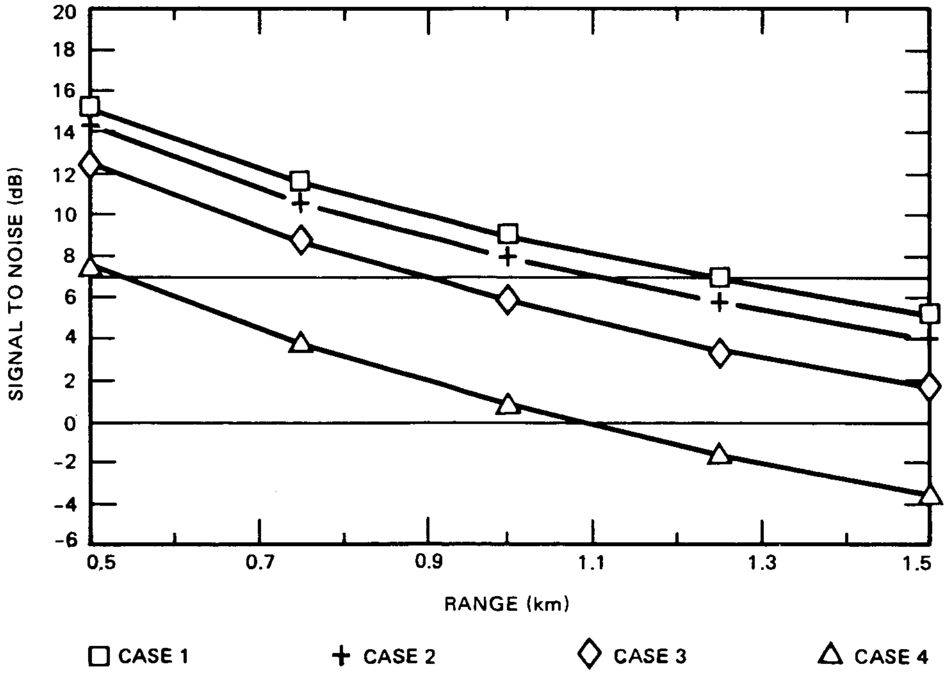

Figure 5-2(b). Calculated performance for 98 GHz with a 12-inch-diameter antenna.

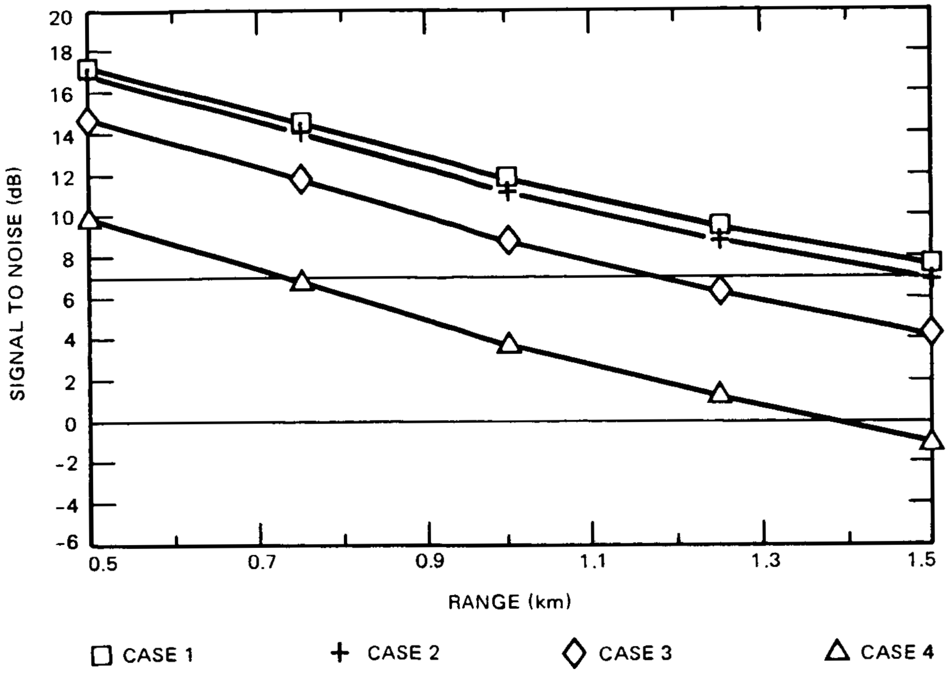

Figure 5-3(a). Millimeter-wave imaging sensor - calculated performance for 140 GHz with a 16-inch-diameter antenna.

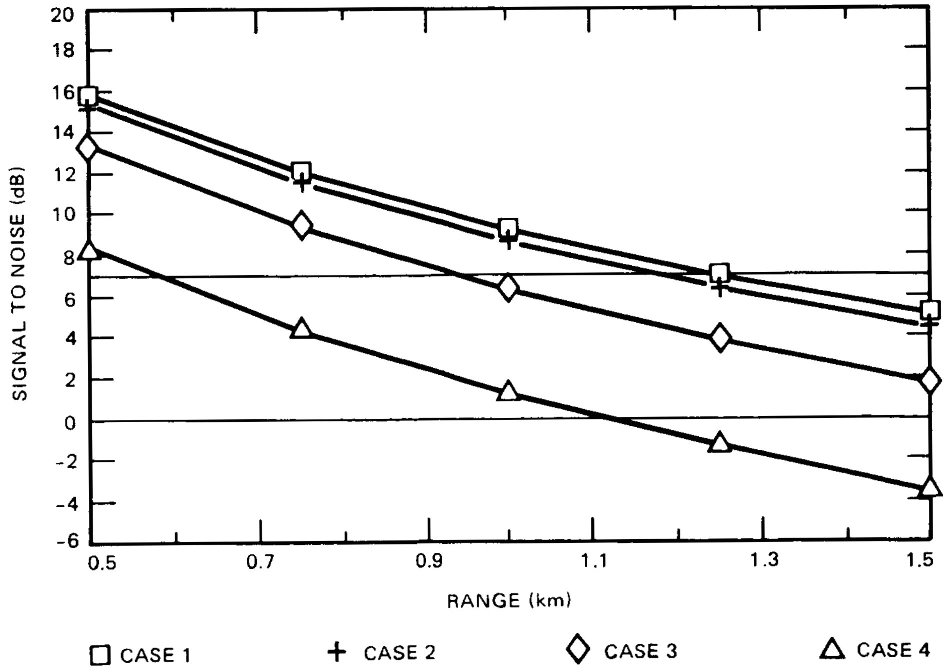

Figure 5-3(b). Calculated performance for 140 GHz with a 12-inch-diameter antenna.

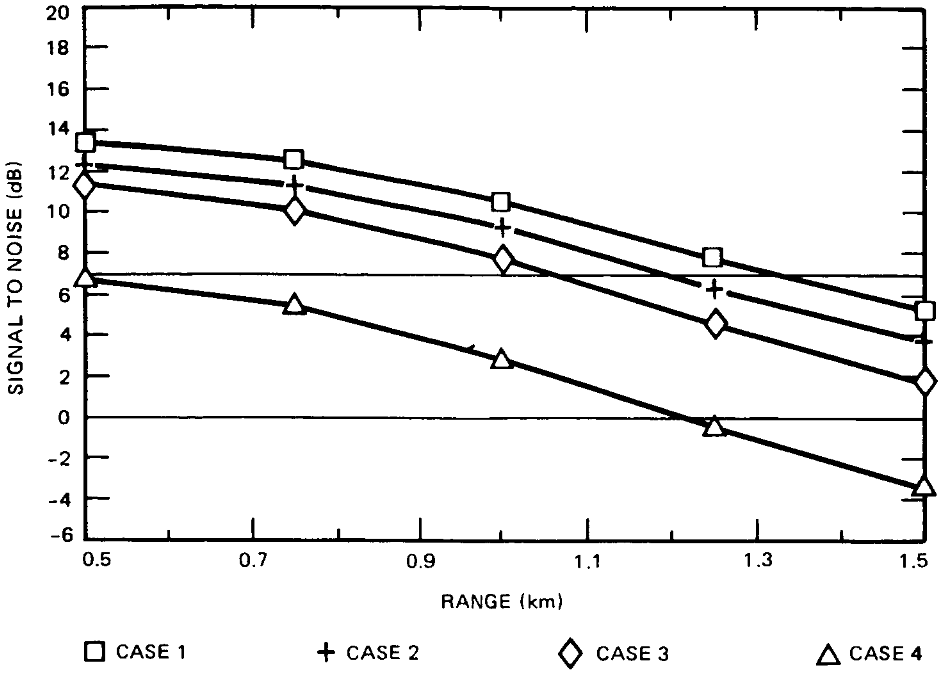

Figure 5-4(a). Millimeter-wave imaging sensor - calculated performance for 220 GHz with a 16-inch-diameter antenna.

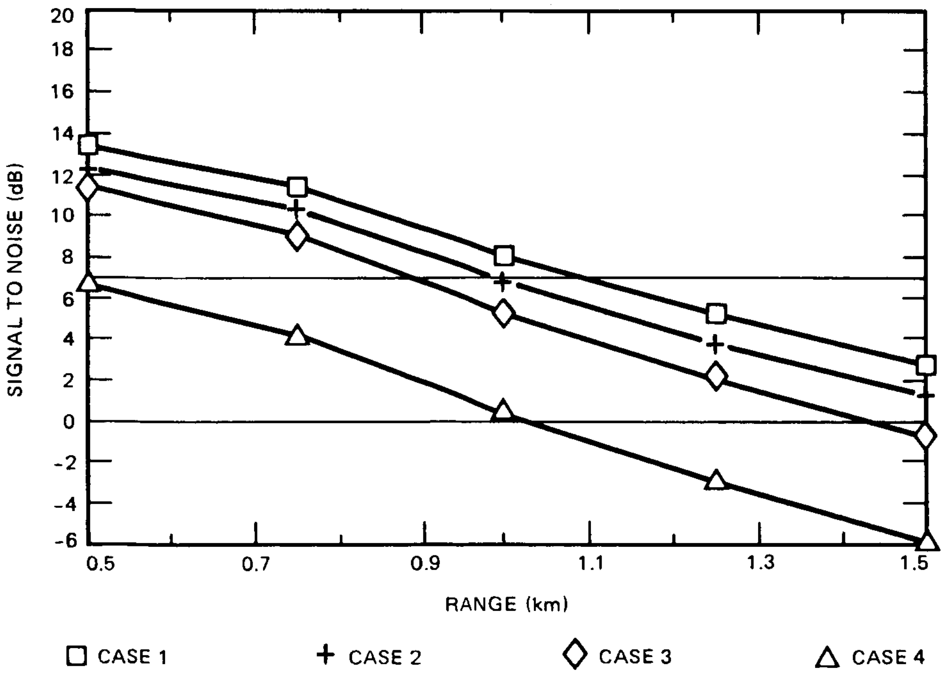

Figure 5-4(b). Calculated performance for 220 GHz with a 12-inch-diameter antenna.

it would be possible to detect tanks with SNRs >5 dB, which will give the 12-inch-diameter system even a larger useful range.

C. MILLIMETER-WAVE AND VISUAL/IR COMPARISON

It is interesting to compare the performance of visual and IR sensors with the mm-wave imager under these poor weather conditions. In Fig. 5-5 there are plotted estimates of the visible/IR attenuation and visibility vs the 3-mm attenuation in fog. The visible/IR estimates were based on data in Ref. 6. Under conditions where the mm-wave sensor works well (the 3-mm attenuation is <1.2 dB/km), both the visible and IR sensors are severely limited in their performance to ranges <300 m. There are large areas in Europe where, in the fall, winter, and spring, the low clouds and fog would prevent operation of visible and IR sensors over 30 percent of the time (Ref. 6); however, the mm-wave sensor would work well.

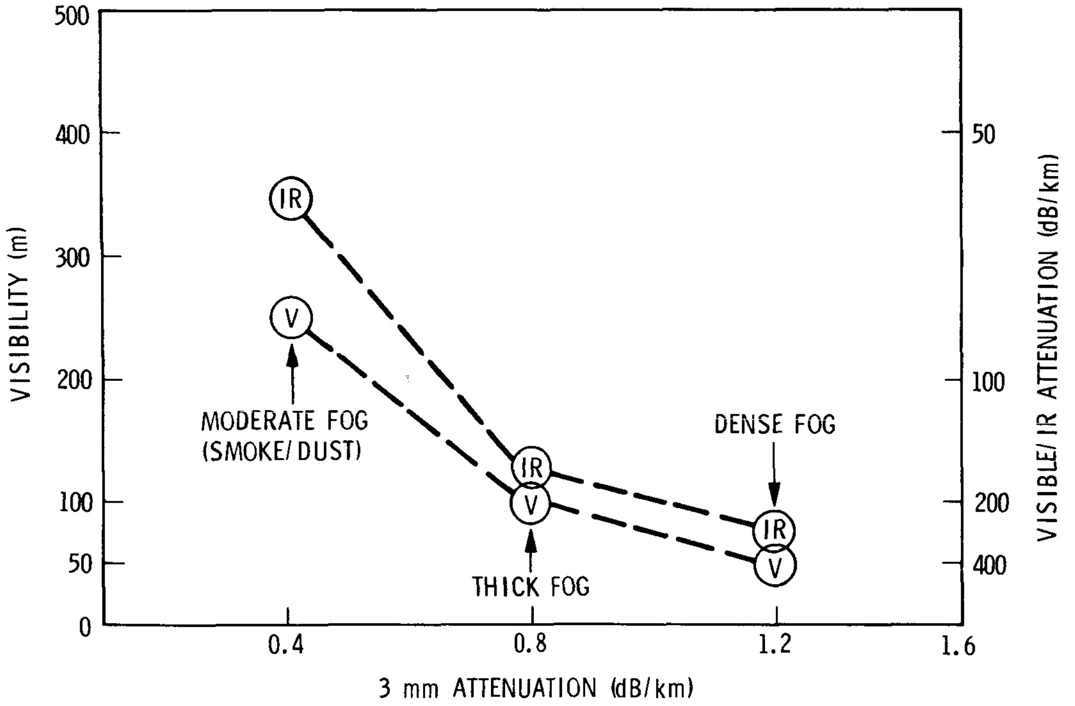

Figure 5-5. Visible and IR attenuation and visibility vs 3-mm attenuation in fog.

D. ANALYSIS AND CALCULATION OF SNR THROUGH VEGETATION COVER

When a mm-wave imaging sensor observes a metal target through vegetation cover, the target's contrast from the background is reduced. However, with moderate vegetation thicknesses, the signal will still be detectable. The effective temperature of the target increases because of the foliage absorbing layer and this increase can be calculated using the equations in section 5A. In these equations, the atmospheric attenuation, L_a, is replaced with the product of the atmospheric and vegetation attenuation $L_a \cdot L_{veg}$. Also the effective sky temperature is increased using the expression:

$$T'_{sky} = \frac{T_{sky}}{L_{veg}} + T_{veg}\left(1 - \frac{1}{L_{veg}}\right), \qquad (9)$$

where

L_{veg} = vegetation absorption

T_{veg} = vegetation temperature (~295 K).

Using the Case 1 weather conditions (clear, moderate fog, smoke or dust), the SNR for a tank vs range was calculated for various values of L_{veg}. These results are plotted in Fig. 5-6.

For these calculations, it was assumed that a 98-GHz mm-wave imager with a 16-inch antenna was used. These calculations show that for $L_{veg} < 2$ dB, the detected signals have SNRs >5 up to ranges of 1 km. This vegetation attenuation of ~2 dB corresponds to moderate foliage thickness of <1 m (Refs. 8-9). Thus, tanks can be detected with a mm-wave imager when located under moderate foliage when the visual and IR sensors would not show any information.

E. SIMULATED LOW SNR IMAGES

It is possible to simulate the mm-wave data with lower SNRs to show

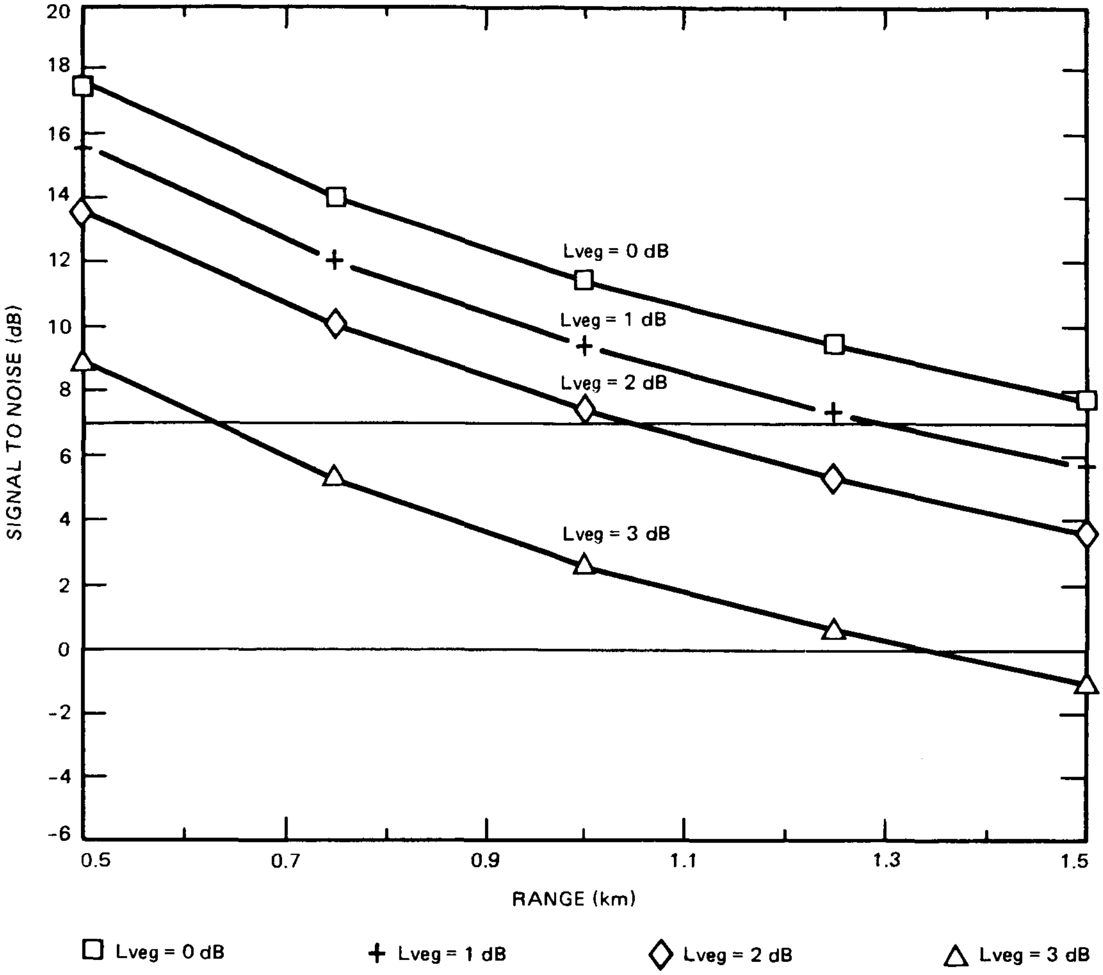

Figure 5-6. Millimeter-wave imager SNR through vegetation

how these data would look under poor weather conditions. This is done by setting a larger temperature range for each color step in the image. The rms noise level, in the original data, is ≈1.6 K. Choosing a 1.5-K color step will show the data with a 1.4-dB reduction in the original SNR. Choosing a 3-K color step reduces the displayed SNR by ~3 dB; a 6-K color step reduces the displayed SNR by ~6 dB, and a 12-K color step reduces the displayed SNR by ~9 dB.

Examples of a few of the images with reduced SNRs are shown in Figs. 5-7 to 5-10 (refer to color figures in Chapter 3). The images are shown with a gray scale to make the comparisons easier. In all the cases, the cold metal reflective targets are easily distinguished. In fact, in the lowest SNR case (-9 dB) the background is much smoother making the cold metal targets stand out. Thus, it seems likely that the mm-wave images will be very usable with the reduced SNR in the poor weather of fog and cloudy conditions.

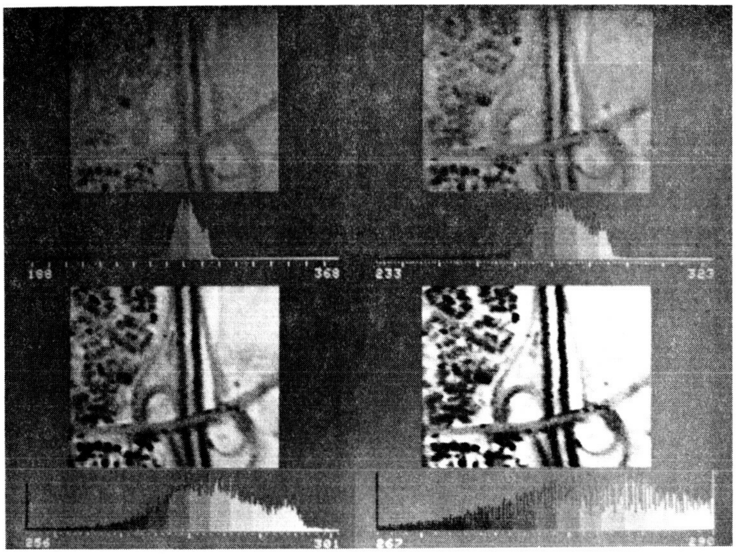

Figure 5-7. Simi Valley Freeway. The UL image has 12-K steps, the UR has 6-K steps, the LL has 3-K steps, and the LR has 1.5-K steps.

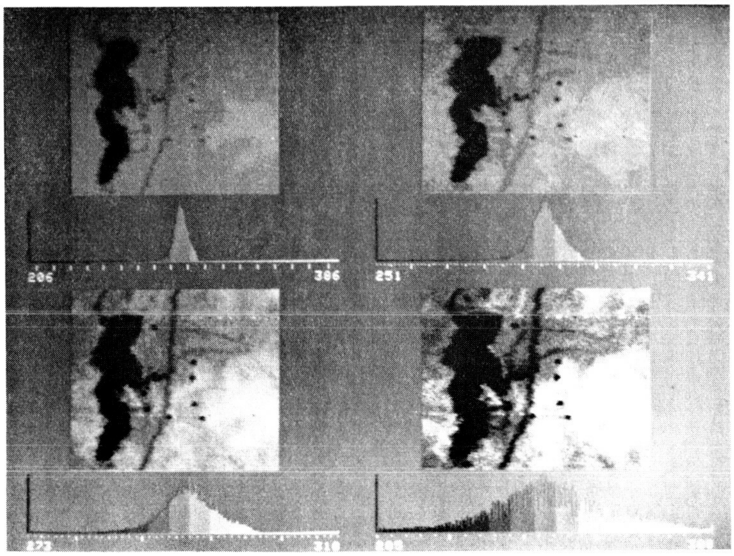

Figure 5-8. Pulgas Lake. The image arrangement is the same as Fig 5-7.

ORIGINAL PAGE IS
OF POOR QUALITY

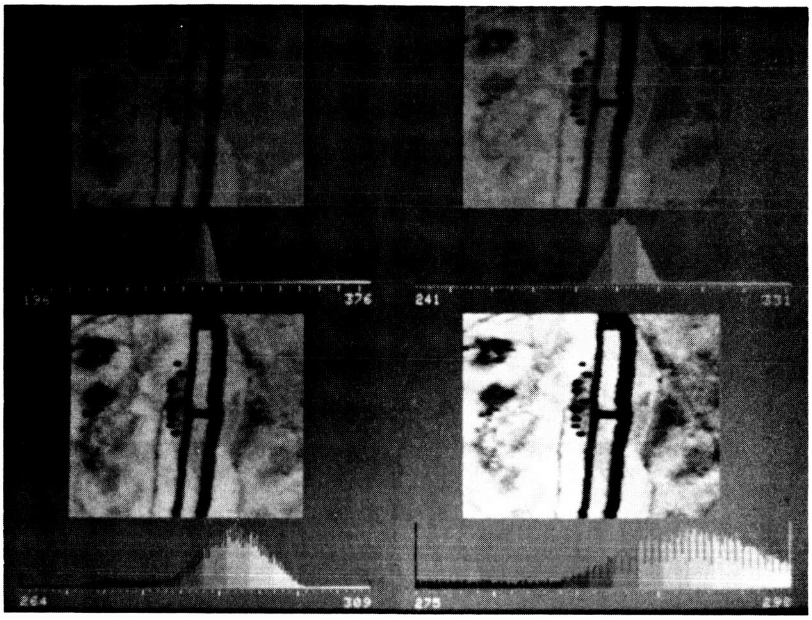

Figure 5-9. Agua Dulce Airport. The image arrangement is the same as Fig. 5-7.

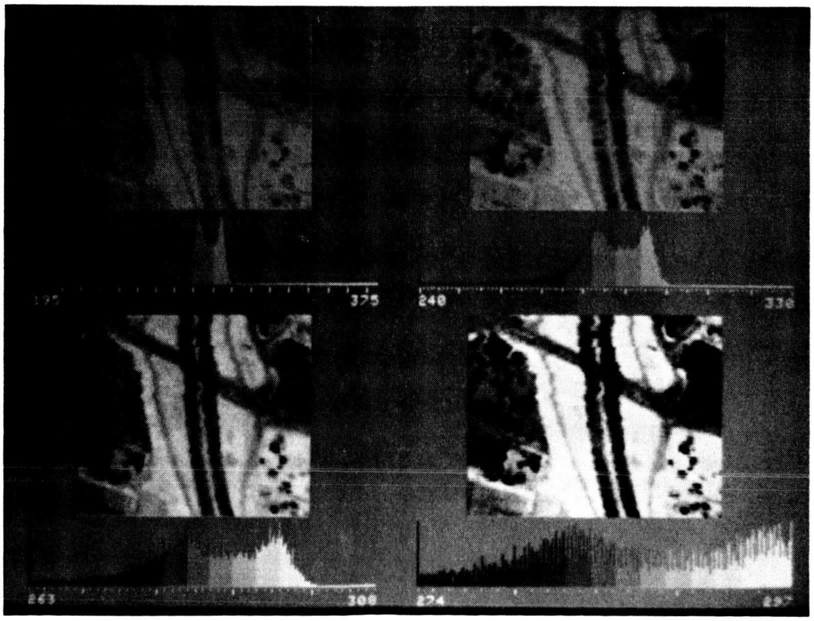

Figure 5-10. I-5 Freeway near Cardiff with clouds. The image arrangement is the same as Fig. 5-7.

REFERENCES

1. Smith, E. K., "Centimeter and Millimeter-wave Attenuation and Brightness Temperature Due to Atmospheric Oxygen and Water Vapor," Radio Science, Vol. 17, p. 1455, Dec. 1982.

2. Tiffany, G. B., "Most Reliable Messenger: mm-Waves Get Through," Microwaves & RF, Vol. 22, p. 64, Sept. 1983.

3. Schuchardt, J. M., Newton, J. M., Morton, T. P., and Gagliano, J. A., "The Coming of MM-Wave Forward Looking Imaging Radiometers," Microwave Journal, Vol. 24, p. 45, Jun. 1981.

4. Liebe, H. J., "Atmospheric EHF: Window Transparencies near 35, 90, 140 and 220 GHz," IEEE Trans. Antennas & Propag., Vol. AP-31, p. 127, Jan. 1983.

5. Clark, W. W., Miller, J. E., and Richardson, P. H., "Sky Brightness Temperature Measurements at 135 GHz and 215 GHz," IEEE Trans. on Antennas and Propag., Vol. AP-32, p. 928, Sept. 1984.

6. Kulpa, S.M., and Brown, E. A., "Near-Millimeter-wave Technology Base Study," Propagation and Target/Background Characteristics, Vol. 1, Harry Diamond Laboratories Report - SR-79-8, p. 4, Nov. 1979.

7. Webb, L. L., Newton, J. M., Foster, M. L., Welch, J. M., Morton, T. P., and Schuchardt, J. M., "Millimeter Wave Passive Target Signature Measurements," Georgia Inst. of Tech., Proj. A-2337, Vols. I, II, Jun. 1980, Jan. 1981.

8. Currie, N. C., Martin, E. E., and Dyer, F. B., "Radar Foliage Penetra-

tion Measurements at Millimeter Wavelengths," Georgia Inst. Tech. Proj. A-1485-100, Dec. 1975.

9. Trebits, R. N., Hayes, R. D., and Domar, L. C., "MM-Wave Reflectivity of Land & Sea," Microwave Journal, Vol. 21, p. 49, Aug. 1978.

CHAPTER 6. PRELIMINARY DESIGN FOR UAV CONFIGURATION

A. INTRODUCTION

In this chapter, a design for a mm-wave imaging sensor, which can be mounted in an Unmanned Aerial Vehicle (UAV) will be described. It will be necessary to reduce the size and weight of the current mm-wave sensor to use it on a UAV. The main changes that will be made are to use a smaller (12-inch-diameter) horn/lens antenna, a smaller crosstrack scan system and to package the equipment around the antenna. Simulated results using this smaller mm-wave imager will also be presented.

B. MILLIMETER-WAVE IMAGER DESIGN FOR UAV

The system specifications for the smaller sensor are shown in Table 6-1. One advantage of using the smaller antenna, with the larger beamwidth $(\Theta_b = 0.7^\circ)$, will be to allow a wider scan angle of ±30° to cover a wider swath width. A drawing of the proposed configuration is shown in Figure 6-1. The sensor weight is estimated to be 120 lb and a breakdown of this

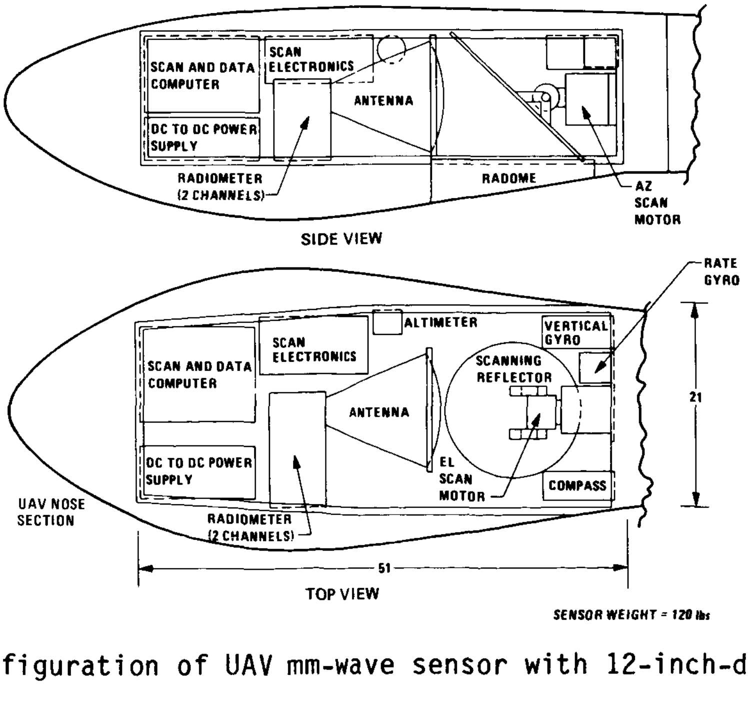

Figure 6-1. Configuration of UAV mm-wave sensor with 12-inch-diameter antenna.

Table 6-1. UAV Millimeter-Wave Imaging Sensor Specifications With 12-Inch-Diameter Antenna

I. SYSTEMS:	
UAV Altitude	750 m (2,460 ft)
UAV Speed	40 m/s (90 mph)
Scan Width	0.9 km (0.5 mi)
Ground Resolution	9 x 9 m
Ground Track	Raster Pattern
Sensitivity: (no clutter)	0.7 K
(1.6 K clutter)	1.7 K
Display Type	False Color TV Image
Area Shown	12.4 x 0.9 km
Pixels per Line	188
Size	21" wide x 14" deep x 51" long
Weight	120 lb
Power	400 watts
Data Rate	25 kbps
II. SCANNING ANTENNA:	
Antenna Type	12" Diameter Horn Lens
Antenna Beamwidth	0.7 deg.
Antenna Beam Efficiency	>90%
Reflector	14" x 18" Elliptical flat
Scanner	2 axis Gimbal
Scan Angle	±30°
Scan Time per Line	0.154 s
Stabilization Type	Gyros with computer
Stabilization Accuracy	±0.1° in 0.15 s

Table 6-1. UAV Millimeter-Wave Imaging Sensor Specifications With 12-Inch-Diameter Antenna (cont'd)

III. RADIOMETER		
Number of Channels		2-orthogonal polarizations
Center Frequency		98 GHz
RF Input Range		94-96 and 100-102 GHz
IF Bandwidth		2 GHz
Local Oscillator		Gunn diode oscillator
Noise Temperature		<800 K (DSB)
Integration Time per Pixel		0.64 ms
Sensitivity per Pixel (with 2-channel average)		<0.7 K
Calibration Type	- Operational	Cal signal at edge of scan
	- Absolute	Hot/Cold loads and vane
Accuracy	- Relative	±1 K
	- Absolute	±5%

estimate is given in Table 6-2. A big savings in weight was made in the scanner where the weight can be reduced from 35 lb to below 25 lb. This estimate was based on an analysis by Sperry Corporation -- makers of the current scanner. Another area where a size and weight reduction can be made is in the computer subsystem. Because of recent advances, it will be possible to shrink the computer to half the size of the one in the present system. As seen in Table 6-2, the power supplies are a major item and it may be possible to reduce their weight.

An estimate of the total power has also been made and was found to be ≈485 watts, which is well within the capability of existing UAVs. A listing of the power requirements is shown in Table 6-3.

No significant developments will be required for the "12-inch" mm-wave imager system, and thus it is estimated that it could be built and interfaced to the UAV, within 24 months after go-ahead.

In Chapter 5, the performance of the 12-inch system for tank detection was predicted to be ~2 dB worse than with the present 16-inch system. This will be satisfactory for surveillance applications for ranges up to 1 km.

C. SIMULATED 12-INCH ANTENNA DATA

To illustrate how imaging data taken with a 12-inch-diameter antenna sensor would appear, it is possible to smooth the existing 16-inch data and then display it. In this smoothing, each pixel is replaced by the sum of itself and the eight surrounding pixels after being multiplied by the following table:

0.03	0.06	0.03
0.06	0.64	0.06
0.03	0.06	0.03

Table 6-2. Estimated Weights for UAV Millimeter-Wave Imager Components

Component	Weight (lb)
Scanner & Mirror*	12.7
Scanner Electronics*	11.1
Horn (worst case)	13.5
Receiver (includes calibration)	10.
Computer	15.
Rate Gyro	2.5
Rate Gyro De-Mod	1.4
Vertical Gyro	2.3
Compass (includes flux det.)	2.0
Scanner Power Supply	4.6
Rate & Vertical Gyro Power Supply	6.1
Receiver Power Supply	5.3
Computer Power Supply	5.3
Structure	28.
Total	119.8 lb

*Based on Sperry estimate

Table 6-3. Power Budget for UAV Millimeter-Wave Imager

Item	V_{DC} (volts)	I_{DC} (amps)	Power* (watts)
Receiver			
	+15	0.6	15.0
	-15	0.1	3.0
	+ 5	1.8	15.0
Computer			
	+12	0.2	4.0
	-12	0.2	4.0
	+ 5	11.0	92.0
Temp Control			
	+28	3.6	100.0
Gyros & Compass			
	+28	2.0	56.0
Scanner			
	+28	7.0	196.0
		Total	485.

*Includes 60%-efficient power converters

This table approximates the weighting of the scene due to the larger antenna beamwidth.

Examples of the lower resolution images are shown in Figures 6-2 to 6-5. The original data are shown in the upper left (UL) image and the smoothed data are shown in the upper right (UR) image. The lower images show enlarged sections of the upper images, with the smoothed version in the lower right (LR) corner. In each case, there is very little change in the 12-inch data and not much detail is lost. As expected, the temperature difference in small objects dropped ~2 dB; however, the entire image is not changed and is perfectly usable. In Fig. 6-2 the Simi Valley Freeway image is shown, and all the vehicles in the 16-inch images are easily detected in the 12-inch images. The tanks near Pulgas Lake are shown in Fig. 6-4, and are easily detected in both the 16-inch and 12-inch images. Thus, from these data, it appears that the 12-inch-diameter antenna system will be satisfactory for surveillance applications.

ORIGINAL PAGE
COLOR PHOTOGRAPH

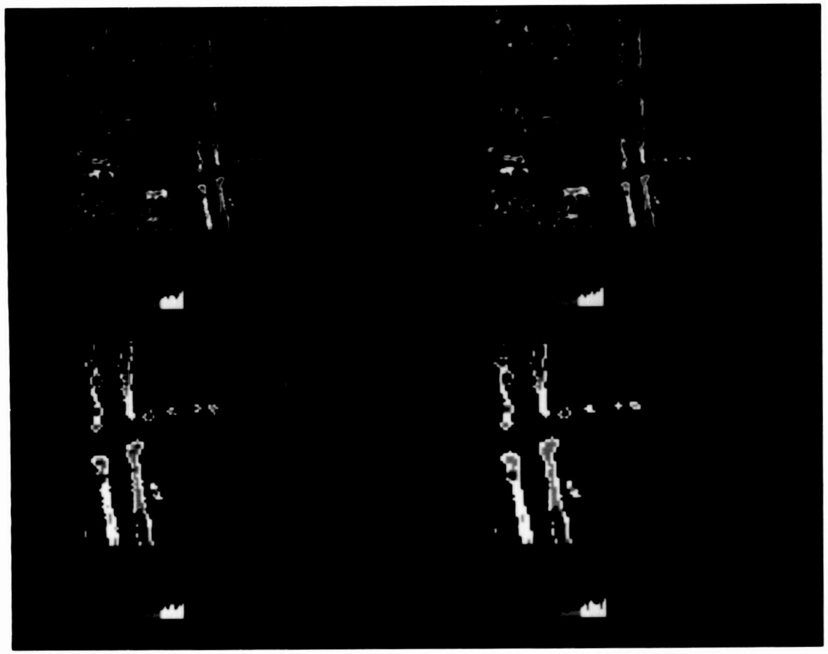

Figure 6-2. Simi Valley Freeway. The UL is the original data, the UR is the 12-inch simulated data. The LL is an enlargement of the UL, the LR is an enlargement of the UR.

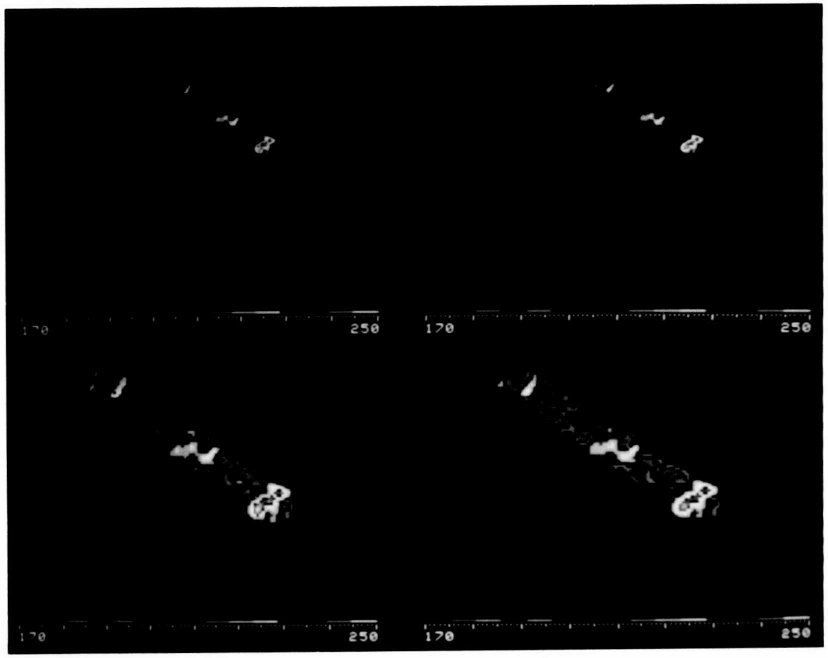

Figure 6-3. Ship in Long Beach Harbor. The layout is the same as in Fig. 6-2.

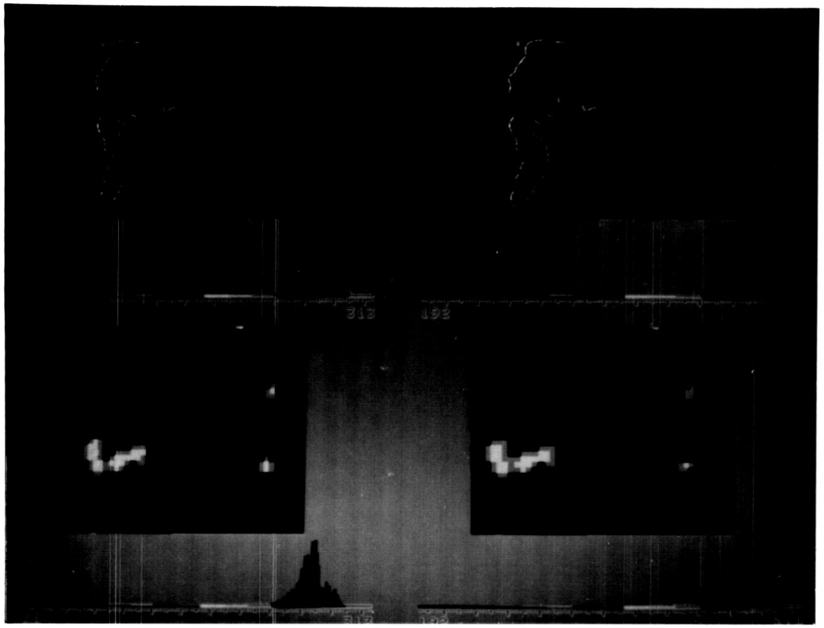

Figure 6-4. Tanks near Pulgas Lake in Camp Pendleton. The layout is the same as in Fig. 6-2.

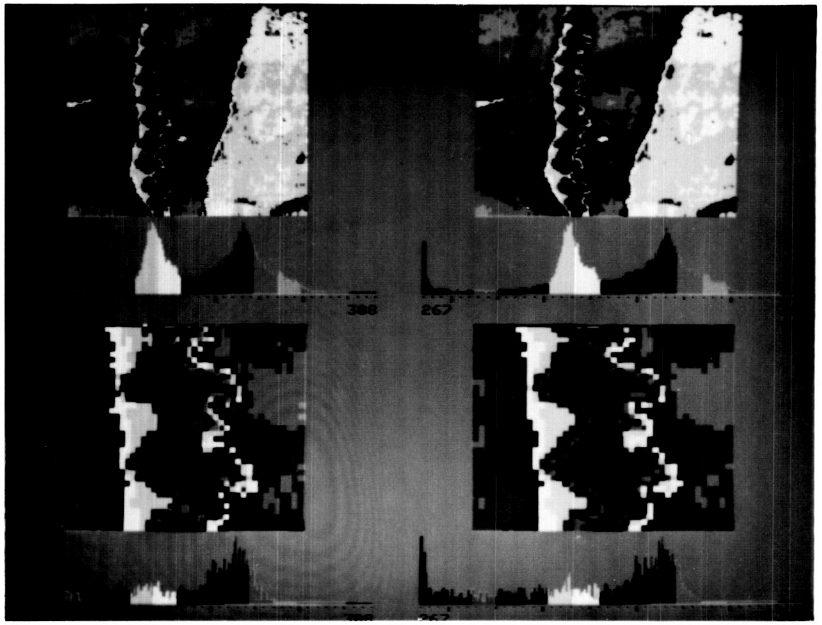

Figure 6-5. Aircraft parked at Mojave Airport. The layout is the same as in Fig. 6-2.

CHAPTER 7. CONCLUSIONS

This report has described the mm-wave imaging sensor and has shown a variety of data taken with the sensor and different ways to display the data to bring out more information. One of the most interesting aspects of these mm-wave images is that there are many recognizable objects; i.e., reflective objects, such as water, metals, highways, and buildings, which stand out from the background "clutter." From a study of many images, it is rare that the temperature range needs to be expanded below 3 K per color step, which is ~4 times larger than the radiometer noise, since the scene "clutter" is ≈2 K. It is also interesting that, by properly choosing the range of temperatures and the order of colors, different features within a scene can be made to "stand out" or "blend" in the picture. Other image processing and enhancement techniques were used to improve object detection and maximize image information as described in Chapter 4.

Using a passive mm-wave imaging sensor for surveillance will be one of its best applications. The image data has poorer spatial resolution than visual or IR sensors; however, there is a tremendous amount of useful information especially for surveillance applications. This is especially true during cloudy and foggy weather when visual and IR images would be blank. Also it is possible to detect metal targets under moderate thicknesses of vegetation when the visual and IR sensors would be unusable. As mentioned in Chapter 4, it will also be possible to use computer target recognition to aid in the real-time use of this data in battlefield situations. Using computers to help analyze the mm-wave imaging data will be necessary for Army personnel in their interpretation of these data. This is an area where further research is required to develop these techniques.

It should be noted that there are many areas in the world where it is cloudy or foggy a significant portion of the time. For example, in central Europe during the fall and winter, it is cloudy and foggy over 30 percent of the time (Ref. 1). During this time, visual and IR sensors would be useless for surveillance. A radar sensor can be used during these cloudy conditions; however, the fact that this active sensor can be detected and then jammed or destroyed puts it at a disadvantage to a passive sensor. Using a radiometer in conjunction with radar, where the radiometer queues the radar for a short look, is an attractive possibility. There is a question on jamming the mm-wave imager, but it should be noted that even if the frequency of the radiometer were known, it would require at least a 3,000-watt transmitter at 100 GHz to jam the mm-wave sensor. (See Appendix B for details of this calculation.) It is unlikely that this capability would ever be practical in a field situation.

In Chapter 5 it was predicted that the mm-wave sensor would work well in a variety of poor weather conditions. The next step in the development of this sensor will be to evaluate its performance under a variety of bad weather conditions to accurately determine the performance limitations. It is estimated that this test program would take about 1 year.

In Chapter 6 a preliminary design for a UAV-mounted sensor was described. In this design no new technology is required, just careful engineering and packaging. If required, this UAV sensor could be built within 24 months.

These are technical improvements in the sensor which are desirable. The main improvement would be the development of a ≈16-inch-diameter electronically scanned antenna with a beam efficiency >90 percent and a loss <2 dB. It is desirable that this antenna be lightweight, relatively small and low cost. Another desired development would be integrated 100-GHz receivers -- to reduce the size and weight of the sensor.

REFERENCE

1. Kulpa, S.M. and Brown, E.A., "Near-Millimeter Wave Technology Base Study," Propagation and Target/Background Characteristics, Vol. I, Harry Diamond Laboratory Report HDL-SR-79-8, Nov. 1979.

APPENDIX A. CONFERENCES AND PUBLICATIONS

This appendix lists the conferences and publications in which the mm-wave imager has been described and the results presented.

A. CONFERENCES

	Conference	Date	Location
1.	DoD/NASA Workshop on Millimeter and Submillimeter Waves and their Applications.	3/11-13/85	Goddard Space Flight Center, Greenbelt, MD
2.	JPL Observational Systems Division Seminar.	6/17/85	JPL, Pasadena, CA
3.	Pecora 10 - Remote Sensing in Forest Management.	8/20-22/85	Colorado State Univ. Ft. Collins, CO
4.	1985 International Geoscience and Remote Sensing Symposium (IGARSS'85) and USNC/URSI Commission F Meeting.	10/7-9/85	Univ. of Massachusetts Amherst, MA
5.	Harry Diamond Laboratory Seminar.	10/10/85	HDL, Adelphi, MD
6.	Aerospace Corporation, Electronics Research Laboratory Seminar.	10/23/85	El Segundo, CA
7.	IEEE 10th Int'l Conference on Infrared and Millimeter Waves.	12/9-13/85	Lake Buena Vista, FL
8.	1986 IEEE MTT-S International Microwave Symposium.	6/2-4/86	Baltimore, MD
9.	Los Angeles IEEE MTT-S Meeting.	6/17/86	Los Angeles, CA
10.	Assoc. for Unmanned Vehicle Systems 1986 meeting.	7/21-23/86	Boston, MA
11.	DoD Conference on Airborne Reconnaissance.	8/21-22/86	Naval Air Station Miramar, CA
12.	JPL Observational Systems Division Seminar.	9/15/86	JPL, Pasadena, CA
13.	Army Research Office Workshop on Fundamental Research Issues in Millimeter/Submillimeter Waves.	9/15/86	UCLA, Malibu, CA

Conference	Date	Location
14. Navy Space Panel-Technology Subpanel.	9/23/86	JPL, Pasadena, CA
15. 1986 Optical Society of America Meeting.	10/19-24/86	Seattle, WA
16. Unmanned Aerial Vehicle Materiel Developer/User Conference.	10/21-22/86	Army Missile Command, Redstone Arsenal, AL
17. JPL/Caltech MM-Wave Seminar.	11/10/86	JPL, Pasadena, CA
18. Dept. of Surveillance & Systems Maintenance at the U.S. Army Intelligence Center & School (USAICS).	11/20/86	Ft. Huachuca, AZ
19. Winter Convention on Aerospace & Electronic Systems	1/27-29/87	El Toro, U.S.M.C. Air Station, Irvine, CA

B. PUBLICATIONS

1. Wilson, W. J., Howard, R. J., Ibbott, A. C., Parks, G. S., and Ricketts, W. B., "Millimeter-wave Imaging Sensor," IEEE Trans. Microwave Theory Tech., V MTT-34, pp. 1026-1035, Oct. 1986.

2. Wilson, W. J., Ibbott, A. C., Parks, G. S., and Ricketts, W. B., "Millimeter-wave Imaging Sensor," Microwave Systems News, V. 16, pp. 94-99, Dec. 1986.

3. Fenstermacher, R., Wilson, W. J., Ibbott, A. C., "Remote Sensing at Milli-Wavelengths - Examples from Owens Valley and Death Valley, CA", (In preparation).

APPENDIX B. MILLIMETER-WAVE IMAGER JAMMING CONSIDERATIONS

The best way to jam the mm-wave imaging sensor would be to make the received signal unstable, thus masking possible targets. A modulated jamming signal with a peak received brightness temperature of >20 K could corrupt the data. In this case, the received jamming power would be:

$$P_{jam} = kTB = 1.4 \times 10^{-23} \times 20 \times 4 \times 10^{9} \text{ watt}$$
$$\cong 1 \times 10^{-12} \text{ watt} = -120 \text{ dBW}$$

To block the received image, it can be assumed that this jamming signal would be coupled into the mm-wave sensor's antenna sidelobes which would have a gain of ~8 dB (~40 dB less than the main lobe). There is also another 3-dB loss since the jamming signal would be polarized and the mm-wave imager has two receivers with orthogonal polarizations which are added. Thus, a jamming signal level of -125 dBW would be required at the mm-wave imager's antenna to jam the signal.

Assuming the line of sight range to the jammer is >10 km, the 100-GHz free-space attenuation loss would be >153 dB. In poor weather conditions when the mm-wave imager would be used, the atmospheric attenuation would be >1 dB/km resulting in an attenuation of >10 dB for the jammer signal. Thus the jammer would need an Effective Radiated Power (ERP) of >+38 dBW. Assuming the jammer uses an "omni" type antenna, with a gain of +3 dB, the jammer must have a peak power of <u>>35 dBW</u> or <u>>3 kW</u> to jam the mm-wave imager.

Another factor, which makes the jamming harder, is that the jammer must know the radiometer frequency within 4 GHz to get into the radiometer's passband. To make this more difficult, the frequency of the radiometer could be selected in the field over a ±10-GHz band by tuning the local oscillator.

At this time, and in the foreseeable future, operational 3000-watt, 80- to 100-GHz transmitters are not practical and thus, it will not be possible to jam the mm-wave imaging sensors.